

CHAPTER I

INTRODUCTION

Developing materials which meet given specifications is a difficult process. For thermoelectrics, this is further complicated due to seemingly contradictory requirements for such materials. A good thermoelectric material should have a high Seebeck coefficient (S), a high electrical conductivity (σ), similar to that of a metal, and low thermal conductivity (κ), similar to that of a glass. As a result, there is strong interest in the development of a fundamental understanding of potential thermoelectric materials and in using theory and modeling to identify promising candidates and to suggest avenues for optimization.

Thermoelectric effects were discovered early in the 19th century. Seebeck discovered the effect that bears his name in 1821 [1]. In this effect, a voltage appears when two different conductors are joined together and the junction is heated. The Peltier effect, discovered in 1834 [1], occurs when an electric current passes through the junction between two conductors. The junction becomes heated or cooled according to the direction of current through it. This reversible effect is usually masked by the irreversible phenomenon of Joule heating. However, it is possible to choose the materials so that the Peltier effect can be used to produce cooling. In 1851, Thomson (later Lord Kelvin) predicted and subsequently observed [1] reversible heating or cooling when an electric current is passed along a single conductor in the presence of a temperature gradient. This is known as the Thomson effect.

In 1911 Altenkirch showed [1, 2] that good thermoelectric materials should possess large Seebeck coefficients, high electrical conductivity, and low thermal

conductivity. A high electrical conductivity is necessary to minimize Joule heating, while a low thermal conductivity helps to retain the heat at the junctions and to maintain a large temperature gradient. Altenkirch introduced the concept of a figure-of-merit (Z), which has ever since assisted researchers in the development of thermoelectric materials. The figure of merit of a thermoelectric material is defined as: $Z=S^2 \sigma/\kappa$ where, S is the Seebeck coefficient of the material (measured in microvolts/K), σ is the electrical conductivity of the material and κ is the total thermal conductivity of the material. The latter can be written as $\kappa=\kappa_L +\kappa_E$ where, κ_L and κ_E are the lattice and the electronic contributions to the thermal conductivity, respectively.

Although the properties favored for good thermoelectric materials have been known for a long time, the advantages of semiconductors as thermoelectric materials were neglected until recently and research continued to focus on metals and metal alloys. These materials, however, have a constant ratio of electrical to thermal conductivity (Weidman-Franz-Lorenz law) so it is not possible to increase one without increasing the other. Metals best suited to thermoelectric applications should therefore possess a high Seebeck coefficient. Unfortunately, most possess Seebeck coefficients of the order of 10 microvolts/K, resulting in thermoelectric generating efficiencies of only fractions of a percent. As early as 1929, when very little was known about semiconductors, Abram Fedorovich Ioffe (1880-1960) showed [3] that a thermoelectric generator utilizing semiconductors could achieve a conversion efficiency of 4%, with further possible improvement in its performance.

A large number of semiconductor materials were being investigated as potential thermoelectrics by the late 1950's and early 1960's, several of which emerged with Z values significantly higher than those in metals or metal alloys. However, no single

compound semiconductor evolved that exhibited a uniformly high figure-of-merit over a wide temperature range, so research focused on developing new materials with high figure-of-merit values over relatively narrow temperature ranges. Of the great number of materials investigated, those based on bismuth telluride, lead telluride and silicon-germanium alloys emerged as the best for operating temperatures of about 450 K, 900 K and 1400 K, respectively.

1.1 Overview of Thermoelectric Materials Research

Ioffe first proposed the investigation of semiconductor materials for utilization in thermoelectric applications [3]. Later, alloys based on the Bi_2Te_3 or $\text{Si}_{1-x}\text{Ge}_x$ systems soon became some of the most widely studied thermoelectric materials. These materials were extensively studied and optimized and to date they remain state-of-the-art materials for their use in specific temperature ranges. Recently, there has been a renewed interest in developing new materials for thermoelectric and other applications. A combination of factors, mainly in the area of alternative refrigeration/power generation and cooling electronics, have led to this current interest. Since the early 1990s, many new classes of materials have been investigated for their potential in thermoelectric applications. The essence of defining a good thermoelectric material lies primarily in determining the material's dimensionless figure-of-merit ZT , where T is the absolute temperature in kelvins. The materials of primary interest are those which contain heavy atoms and are also relatively easy to dope to tune the electronic properties. The best thermoelectric materials currently have $ZT \sim 1$ [2]. However, there is no fundamental reason why this value cannot be larger. One of the goals of current research is to achieve $ZT \sim 2-3$.

Considerable attention has been given to the bismuth-antimony (Bi-Sb) alloys for thermoelectric applications [4-6]. Smith and Wolf (1962) [7] first studied the $\text{Bi}_{1-x}\text{Sb}_x$ alloys as potential materials for electronic refrigeration. They reported that *n*-type Bi-Sb alloys had higher *ZT* than the Bi_2Te_3 alloys in the temperature range 20-220 K. However, the immediate application of Bi-Sb alloys were constrained due to the lack of suitable *p*-type material with compatible properties that could be incorporated into a single thermoelectric device. Later, Goldsmid et al. (1988) [8] showed that a *p*-type high- T_c superconductor can have a similar *ZT* as the *n*-type Bi-Sb alloys. Over the years there has been a great volume of work done on the unique properties of Bi-Sb alloys. Despite these efforts, there has been no significant improvement in the figure-of-merit of the Bi-Sb alloys since the first work by Smith and Wolf.

Half-Heusler alloys have also emerged as potential thermoelectric materials. A group of compounds having the formula MNiSn ($\text{M} = \text{Ti, Zr, Hf}$) were found to be semiconducting with band gaps in the range 0.1-0.2 eV [9]. These alloys also exhibited large Seebeck coefficients and moderately high electrical resistivity [10, 11]. Soon this type of half-Heusler compounds became important materials in thermoelectric research. Recent studies have revealed many important electrical and thermal properties of these materials [12, 13]. The typical *ZT* of these materials is ~ 0.6 at 800 K. The best thermoelectric materials currently have *ZT* close to unity. This underscores the importance of half-Heusler alloys as potential thermoelectric materials. Their performance may be further enhanced by reducing the lattice contribution of the constituent elements to the thermal conductivity.

Quasicrystals are another class of very important materials for thermoelectric purposes. After their first synthesis in 1984 [14], quasicrystals remain one of the most

fascinating materials. They are characterized by their unique structure as well as properties such as high mechanical strength and low thermal conductivity over a broad temperature range. Quasicrystals have thermal conductivities that are below 10 W/m-K between 2-1000 K, with room temperature values typically within 2-3 W/m-K [15]. This obviously caught the attention of the thermoelectric research community. Theoretical predictions indicate high ZT values may be possible in these materials [16]. However, studies on the tunability of the electrical properties and the Seebeck coefficient and the effect of compositional changes on the material properties are needed in order to fully understand the feasibility of quasicrystals in thermoelectric applications.

Much of the current research on thermoelectric materials has revolved around the concept of the “phonon glass-electron crystal” model (PGEC) which was proposed by Slack [17]. This concept suggests that good thermoelectric materials should have the electronic properties of a crystalline material and the thermal properties of a glass. One promising class of materials that fit the PGEC concept is the Group IV semiconductor clathrates.

Clathrates are mainly classified into two categories: type I and type II. The type I Ge clathrates, for example, are based on compounds having formula A_8Ge_{46} where “A” represents guest atoms within voids in the Ge network. One particular material with the composition $Sr_8Ga_{16}Ge_{30}$ (Nolas et al., 1998) [18] has a lattice thermal conductivity at room temperature that is less than twice that of amorphous Ge. Similarly, low thermal conductivities have been reported for Ge clathrates containing other elements such as Eu (Cohn et al., 1999) [19]. Similar work has been done on Si [20] and Sn clathrates [21, 22]. Some of the clathrates have high Seebeck coefficients and a dimensionless figure-

of-merit approaching unity at about 700 K. The detailed properties of these materials will be discussed in a later chapter.

For several years, work has also been done on materials known as skutterudites. Binary skutterudites have the chemical formula MX_3 where $M = \text{Co, Ir, Rh}$ and $X = \text{P, As, Sb}$. A major feature of the crystal structure of these materials is two large empty spaces (called “cages”) within the unit cell. Some skutterudites have large Seebeck coefficients of the order of ± 200 microvolts/ K, but the thermal conductivity is generally large. However, the lattice thermal conductivity (κ_L) can be substantially reduced by introducing heavy atoms into the spaces in the lattice. This has been successfully done, for example, by Nolas et al. (1998) [23] who added La to CoSb_3 . In this case, it was found that the lattice thermal conductivity was reduced by an order of magnitude at room temperature. Reason for this reduction was due to the scattering of the lattice phonons due to “rattling” of the loosely bound atoms in their “cages”. A dimensionless figure-of-merit of about unity has been observed for these materials at 700 K.

There are other systems that show promise for thermoelectric applications. One of the recent proposals was that the figure of merit might be improved if two-dimensional structures were used [24]. It is possible that a one dimensional system will be better still. However, it is not clear how low dimensional systems can be incorporated within practical devices.

1.2 Motivation for this Work

Among the different types of materials investigated, open framework Si and Ge clathrates have been the subject of considerable interest in recent years. This is mainly

due to structural characteristics that give rise to their unique electrical and thermal transport properties [2]. There are two structural clathrate phases: (i) Type I is a simple cubic structure in which 20-atom cages (pentagonal dodecahedra) and 24-atom cages (tetrakaidecahedra) are combined periodically in a 2 to 6 ratio. (ii) Type II has a face centered cubic (fcc) structure in which 20 and 28-atom cages (hexakaidecahedra) are combined periodically in a 4 to 2 ratio. The cubic unit cell contains 46 atoms and 136 atoms in the type I and type II structures, respectively [25]. The clathrate framework cages can host guest atoms, which are usually alkali or alkaline earth atoms. This unique structural feature has generated considerable experimental and theoretical interest.

The type II clathrate unit cell has two different sized cages (dodecahedra and hexakaidecahedra) which can host the alkali or alkaline earth metal guest atoms. These guest atoms, also known as “rattlers”, due to their low frequency vibrational modes, are loosely bound inside the cages. Their localized vibrations may also scatter the heat carrying phonons of the host framework [26-28], which may contribute to a reduction in the lattice thermal conductivity. The guest atoms may also significantly alter the electronic properties of the host material. Most filled type II clathrates are metallic [29, 30]. This means that the electronic contribution to the thermal conductivity could be large and hence such materials are not very useful as thermoelectrics.

The main reasons for the continued interest in this compound class are (i) theoretical studies and experimental syntheses of guest filled Si and Ge clathrates showing that they have glass-like thermal conductivity [17, 19, 31, 32], (ii) the prediction and demonstration of electronic properties ranging from poorly semiconducting (low guest content) to semi-metallic (high guest content) behavior [33-36], and (iii) the discovery of superconductivity in $\text{Na}_x\text{Ba}_y\text{Si}_{46}$ clathrates [37].

The type II clathrates have been relatively less investigated compared to the type I variety. The most interesting aspect of type II clathrates is that the guest atom concentration in the two different cages may be varied from 0 to 24 per unit cell. There is a need for continued research on this type of materials to gain better insight of their properties, which may lead to potential applications in semiconductor, superconductor, thermoelectric and opto-electronic devices.

First principles methods have been used in this work to explore the properties of several type II materials. This work has investigated the structural, electronic, and vibrational properties as well as some thermodynamic properties of these materials using an approach based on density functional theory. The calculations have been carried out within the local density approximation (LDA). A hope is that these calculations will be used as a complementary tool to experimental investigations. Many experimental groups have recently started to use band structure calculations to sift through various compounds with the goal to find new thermoelectric materials [2, 38-40]. Wherever possible, our predicted results have been compared with available experimental data with the goal of better prediction of materials properties from first principles calculations.

CHAPTER II

GROUP IV TYPE II CLATHRATES

The word “clathrate” is derived from the Latin word “clathratus” meaning enclosed or protected by cross bars of a grating. It is presently used in chemistry to describe a particular type of compound where one component forms a cage structure in which atoms or molecules of another component of appropriate size are entrapped. These inclusion structures have been known for many years as naturally occurring hydrates of some species, where crystalline complexes of water form clathrate compounds with simple molecules such as chlorine (Cl_2). This type of compounds has been known for more than a century [41]. Subsequently, many different clathrate hydrates have been synthesized in the laboratory with different inclusion materials such as noble gases, low molecular weight hydrocarbons etc.

In the 1960s, Cros and co-workers [25, 42, 43] reported the existence of two clathrate phases comprised of Group I and Group IV elements, viz. $\text{Na}_8\text{Si}_{46}$ and $\text{Na}_{24}\text{Si}_{136}$. These were synthesized in the laboratory and had structures similar to the well known clathrate hydrates. Later, in a pioneering work, Cros et al. reported on the high temperature electrical properties of $\text{Na}_x\text{Si}_{136}$ [44].

The type II clathrate has a face centered cubic (fcc) unit cell. There are 34 atoms per fcc unit cell. The cubic unit cell has 136 atoms. The pure clathrates are a fourfold coordinated open framework structure comprised of face sharing polyhedra. Two types of polyhedra, namely a pentagonal dodecahedron (20 atom cage formed by 12 pentagonal faces) and a hexakaidecahedron (28 atom cage formed by 12 pentagonal and 4 hexagonal

faces), form the building blocks of these materials. Figure 2.1 shows the two different polyhedral building blocks of the type II clathrate structure [35]. Sixteen pentagonal dodecahedra and eight hexakaidecahedra combine periodically to form the 136 atom cubic unit cell. There are twenty four cavities in total per cubic unit cell, which may host guest atoms.

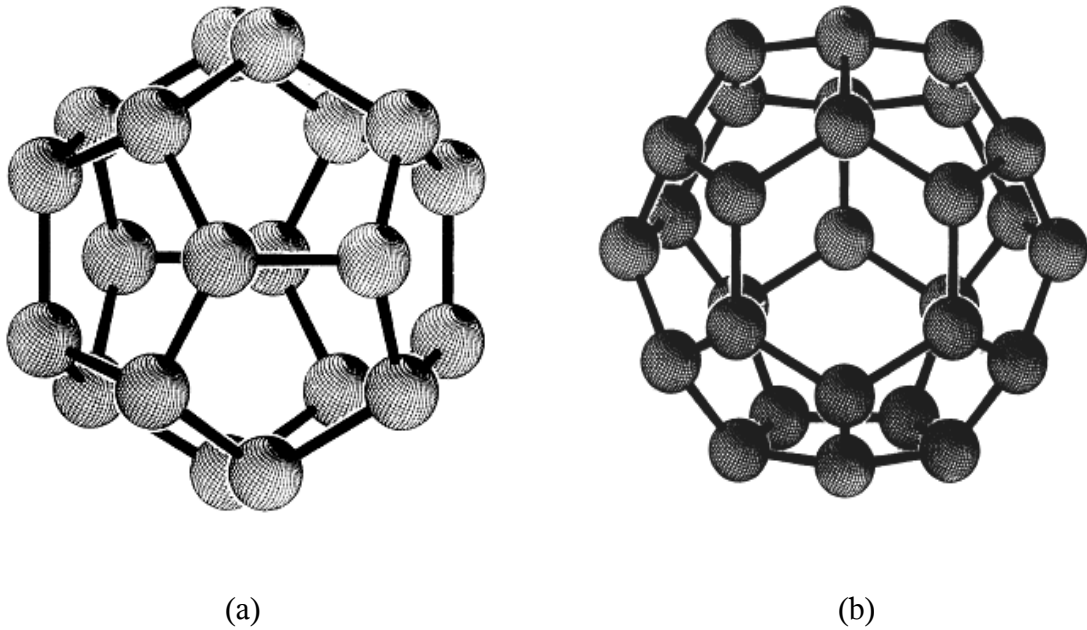


Figure 2.1: Polyhedral building blocks of type II clathrate (a) pentagonal dodecahedron having 12 faces and (b) hexakaidecahedron having 16 faces [35].

The type II structure is represented by the general formula $X_8Y_{16}E_{136}$, where X and Y are typically alkali-metal or alkaline-earth guest atoms filling up the twenty four cavities in the unit cell. E represents a Group IV element Si, Ge, or Sn. However, the occupancies of the X and Y atoms may be less than 8 and 16 respectively, in the cubic unit cell. This would mean only a partial occupancy of the voids. Figure 2.2 is a schematic of the type II $Na_{24}Si_{136}$ clathrate. The framework Si atoms are represented by the dark small spheres and the guest Na atoms by the lighter spheres [45].

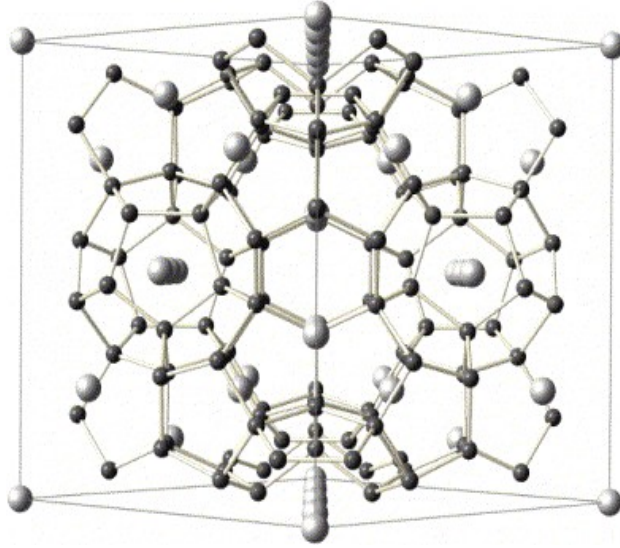


Figure 2.2: Schematic representation of the $\text{Na}_{24}\text{Si}_{136}$ clathrate. The dark spheres represent the Si atoms and the light spheres represent the Na atoms [45].

The clathrate framework is formed by distorted tetrahedral covalent bonding of the Group IV atoms (Si, Ge or Sn). The bond angles may range from 105° to 126° [1], and the average is close to the perfect tetrahedral angle of 109.5° . The guest atoms are interstitially placed inside the cages and are loosely bound with the host framework atoms.

As mentioned earlier, Cros and co-workers [42, 43] reported in the 1960s about the existence of both type I and II clathrate phases of Si and Ge. For a long time not much attention was paid to these materials except a few studies on their structural, electrical and magnetic properties [33]. Following the demonstration of the phonon glass-electron crystal concept (PGEC), there has been a renewed interest in these open-structured semiconducting compounds. Since the mid 1990s there has been a resurgence both in theoretical and experimental work done on the Si, Ge and Sn clathrates.

Adams et al. (1994) [46] reported a theoretical study on the structural and electronic properties of the Si clathrates. Using an approximate tight-binding-like molecular dynamics method, they found an indirect band gap of 2.4 eV for Si_{136} compared to 1.7 eV in diamond structured Si (*d*-Si). Using a plane-wave basis, they found an indirect band gap of 1.4 eV for Si_{136} and 0.7 eV for *d*-Si. In either case there is an enormous opening of the band gap for the Si_{136} phase compared to that of *d*-Si. This widening of the band gap could have useful optoelectronic applications. They also noted that the total binding energy of the clathrate phase was only 0.07 eV/atom higher than the *d*-Si phase, whereas the volume increase in the clathrate phase was about 17%.

The LDA calculated band gap of Si_{136} is approximately 1.2 eV [47]. However, LDA is known to under estimate band gaps. Using the GW quasiparticle approach it has been shown that the band gap for Si_{136} opens up to 1.9 eV [48].

Smelyansky et al. (1997) [36] reported on the theoretical study of the electronic structure of $\text{Na}_x\text{Si}_{136}$ for $x = 0, 4, 8, 16$ and 24 . They showed that at low Na concentration ($\text{Na} \leq 8$), the Si clathrates behave either as an insulator or a semi-metal. The metallic character became prominent with increasing Na concentration. They postulated that, at low Na concentration, when the large hexakaidecahedra cages were preferentially occupied, the interactions between the framework and the alkali metal remained small and there was no charge transfer from the metal atom to the host framework, resulting in an insulator or semi-metal type behavior. At high Na concentration there was a definite charge transfer from the metal atom to the Si framework, resulting in a metallic behavior.

A complete theoretical study of the electronic and vibrational properties of the empty Si and Ge clathrates was done by Dong et al. (1999) [47, 49]. Using density functional theory within the local density approximation (LDA), they predicted the

electronic band structure and the phonon dispersion relations of these materials. As previously seen in Si clathrates, the total binding energies of the Ge clathrates were only 0.04-0.05 eV/atom higher than the ground state diamond phase, while their volumes expanded by about 13-14%. The phonon dispersion curves showed acoustic modes below about 100 cm^{-1} and 60 cm^{-1} for Si and Ge clathrates respectively. For the Si clathrates the highest frequency optic modes shifted downwards by about 30 cm^{-1} compared to the silicon diamond phase. This frequency downshift was attributed to the topology of the clathrate framework, mainly the presence of the five membered rings.

Meanwhile, during the late 1990's, many important experimental discoveries were being made. Mélinon et al. (1999) [50] reported the experimental observation of the full vibrational density of states in the two Si clathrate phases. The phonon density of states was measured using inelastic neutron scattering at 300 K. The reported spectra had three distinct regions. A low frequency region, attributed to the acoustic modes (AM), a medium frequency region due to some acoustic and mostly optic modes ((A+O)M), and a high frequency optic mode (OM) region. They also observed a slight frequency downshift of the optical branches towards lower energy in the clathrate phase compared to the diamond phase. This frequency downshift was also observed in phonon dispersion relations obtained from first principles calculations [47].

The temperature dependence of the lattice thermal conductivity (κ_L) of filled Ge clathrates was measured by Nolas et al. [32]. At low temperatures ($< 3\text{-}4$ K), the data indicate a T^2 dependence, which is reminiscent of the thermal conductivity of amorphous materials. At higher temperatures, the thermal conductivity shows a minimum or a dip. It was postulated that this “resonance dip” in κ_L of the filled clathrates was due to the resonant scattering of host acoustic phonons by the localized vibrational modes of the

guest atoms. However, this may not be entirely true as shown in recent studies and also seen from our estimated Einstein temperatures, which will be discussed in Chapter VI. Figure 2.3 shows experimental results for the lattice thermal conductivity κ_L , as a function of temperature for the $\text{Na}_1\text{Si}_{136}$ and $\text{Na}_8\text{Si}_{136}$ clathrates [45]. There is a noticeable dip in κ_L at about 70 K for $\text{Na}_8\text{Si}_{136}$. The temperature dependence of the lattice thermal conductivity for *d*-Si is shown for comparison (dashed curve).

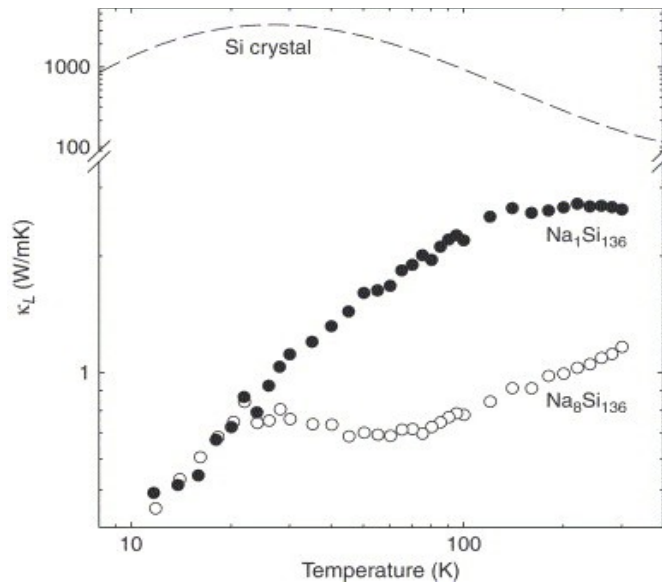


Figure 2.3: Experimental temperature dependence of the lattice thermal conductivity (κ_L) of $\text{Na}_1\text{Si}_{136}$ (solid circles) and $\text{Na}_8\text{Si}_{136}$ (open circles). Also shown is the temperature variation of κ_L for crystalline Si (dashed curve)[45].

Nolas et al. (2003) [51] also reported on the thermal properties of the guest free Si_{136} . The magnitude of its thermal conductivity at room temperature was reported to be slightly larger than that of amorphous silica and about thirty times lower than that of diamond phase silicon [51]. The low value of the lattice thermal conductivity in Si_{136} cannot be described by the phonon scattering mechanism due to “rattling” atoms. This

means the rattling guest atoms inside the cages is not the only mechanism that reduces the thermal conductivity of the clathrate materials. The huge difference in the thermal conductivities between the two phases of silicon could be related to the flattening of the phonon dispersion relations associated with formation of the low density structure of Si_{136} .

Variable temperature single-crystal diffraction measurements of various filled type II Si and Ge clathrates were also reported by Nolas et al. (2002) [30]. They found strong temperature dependence of the atomic displacement parameters (ADP) for the alkali metal atoms in $\text{Na}_{16}\text{Cs}_8\text{Si}_{136}$, $\text{Na}_{16}\text{Rb}_8\text{Si}_{136}$, $\text{Na}_{16}\text{Cs}_8\text{Ge}_{136}$ and $\text{Na}_{16}\text{Rb}_8\text{Ge}_{136}$. The ADP is a measure of the mean-square displacement amplitude of an atom about its equilibrium lattice site. Thus the magnitude of the ADP depends on how “vigorously” the atoms are vibrating. The high values of the ADP is indicative of the “rattling” of the guest atoms inside the two different sized polyhedra of the clathrates. It is important to note that the Cs atom, although heavier than Rb, has been shown to have a lower ADP [30]. Our calculations agree with this result (see Chapter VI). This could be important in choosing the right “rattler” atoms in order to achieve optimum material properties. The localized dynamic disorder created by the guest atom should lead to even lower thermal conductivities for the guest filled type II clathrates compared to that for Si_{136} . However, thermal conductivity measurements reveal quite large values for the filled type II specimens. The thermal conductivity of $\text{Na}_{16}\text{Cs}_8\text{Ge}_{136}$, for example, was lower than diamond structured Ge but much higher than the filled type I clathrates such as $\text{Sr}_8\text{Ga}_{16}\text{Ge}_{30}$ [30]. This is due to the metallic nature of all these type II clathrates which resulted in an increased electronic contribution to the total thermal conductivity.

The above discussion provides a short review of some of the work done so far on the Si and Ge type II clathrates. The next chapter will give a brief outline of the present work on some of these materials.

CHAPTER III

DESCRIPTION OF CURRENT WORK

In the past decade, tremendous effort has been made towards increasing the understanding of the properties of the Group IV clathrates. This has led to huge advancements in our current knowledge about these materials. However, more progress has to be made in order to optimize these materials for various applications including thermoelectrics.

One goal of the current work was to look for explanations for some of the experimental observations, particularly the temperature dependent Knight shift as observed in some filled type II clathrates [29, 52]. Another consideration was to use the results from first principles calculations to predict measurable material properties and to compare those with available experimental data. The goal is to better predict material properties using first principles calculations, which can serve as an effective tool for experimentalists towards optimizing this class of materials.

The materials that were chosen for this work are listed in Table 3.1. Results for Si_{136} and Ge_{136} have been widely reported before [47, 49]. So the initial aim was to reproduce previous results based on our plane-wave calculations. To the best of our knowledge there have been no other theoretical studies reported on the rest of the materials considered here. There is experimental data available on some these filled clathrates, which provides the opportunity to complement the theoretical results with available data.

First part of this work is concerned with the structural properties and the energetics of these materials. After the structural optimization process, a subsequent

fitting of the calculated total binding energies at various volumes to the Birch-Murnaghan equation of state [53] provides the minimum equilibrium energy, the corresponding volume at minimum energy and the bulk modulus of the various materials. The equilibrium volume can be used to find the lattice constant which may be compared with available experimental values.

Table 3.1: List of the different type II Si and Ge clathrates that are reported in this work.

Si Clathrates	Ge Clathrates
Si ₁₃₆ , Na ₁₆ Rb ₈ Si ₁₃₆ , K ₁₆ Rb ₈ Si ₁₃₆ , Rb ₈ Ga ₈ Si ₁₂₈ and Cs ₈ Ga ₈ Si ₁₂₈	Ge ₁₃₆ , Na ₁₆ Rb ₈ Ge ₁₃₆ and Na ₁₆ Cs ₈ Ge ₁₃₆

Second part of this work focuses on the electronic band structure of these materials. The band structure results give important information about the electronic properties of a material, including the predicted band gap. Some of the filled clathrates show large temperature dependent Knight shifts [29, 52]. Gryko et al. has reported the temperature dependence of these shifts in Na_xSi₁₃₆ ($7 \leq x \leq 9$) [54]. Lattturner et al. reported similar temperature dependent shifts in Na₁₆Rb₈Si₁₃₆ [29]. The most interesting feature observed was the fact that these shifts increased with decreasing temperature. This strong temperature dependence is very different from the Knight shift observed in metals, where it is approximately temperature independent. One portion of this work focuses on the calculations which provide an explanation of these observed Knight shifts. It is shown that the results for the electronic density of states of these materials provide a qualitative explanation for this behavior.

Framework substitution has not been widely reported among the type II clathrates. Thus far, one published work is available on framework substitution in type II clathrates, where some of the Si framework atoms were substituted by Ge with no guest atoms occupying the cages [55]. Most non-framework substituted filled (partially or completely filled) type II clathrates are metallic. This metallic behavior could mean a larger electronic contribution to the total thermal conductivity, as seen from the thermal conductivity data for $\text{Na}_{16}\text{Cs}_8\text{Ge}_{136}$ [30].

The electronic properties of some framework substituted clathrates viz. $\text{Rb}_8\text{Ga}_8\text{Si}_{128}$ and $\text{Cs}_8\text{Ga}_8\text{Si}_{128}$, have been reported here. The framework substituted $\text{Rb}_8\text{Ga}_8\text{Si}_{128}$ and $\text{Cs}_8\text{Ga}_8\text{Si}_{128}$ clathrates were found to be semiconducting with smaller indirect band gap than pristine Si_{136} . This semiconducting property could potentially reduce the electronic contribution to the thermal conductivity.

Next part of this work focuses on the vibrational properties of these materials. The phonon dispersion relations show low frequency localized vibrational modes of the guest atoms. Using the calculated frequencies in the harmonic approximation, we have estimated the effective force constants of the various guest atoms. Based on these estimated force constants we have predicted the temperature dependent mean square displacement amplitude of the various guest atoms (U_{iso}). These values of U_{iso} were compared with the experimentally obtained atomic displacement parameter (ADP) for some of these materials. Our predicted U_{iso} are in fairly good agreement with some of the experimental values of the ADP.

There has been a dearth of studies on the thermodynamic properties of the Group IV clathrates. Most results reported so far have focused on the synthesis and structural and transport properties of these materials [2]. Many theoretical studies have concentrated

more on the electronic band structure and vibrational properties of clathrates. Studies of the fundamental thermodynamic properties remain limited. These studies could be important in order to fully understand the unique properties of the expanded phase semiconducting clathrate materials.

The vibrational results were used to calculate the lattice contributions to the thermodynamic properties (free energy, entropy and heat capacity at constant volume) of the empty Si_{136} and Ge_{136} clathrates. Thermodynamic properties of Si_{136} using the harmonic approximation and the Tersoff potential [56] have been reported earlier [57]. However, the *ab initio* calculations performed in this work are more accurate and compared better with experimental data than those earlier reports. Our predicted temperature variation of the heat capacity of Si_{136} is in good agreement with experimental results [58]. The temperature dependence of the heat capacity of both Si_{136} and Ge_{136} is found to be similar to that of diamond structured Si and Ge, respectively, in the temperature range considered.

CHAPTER IV

COMPUTATIONAL DETAILS

In this study, total energies, electronic band structures and densities of states were calculated using density functional theory (DFT), in which the self-consistent Kohn-Sham equations [59] are solved in the local density approximation (LDA). The materials considered have a face-centered cubic (fcc) structure and have the same symmetry as their “parent” (Si_{136} or Ge_{136}) framework lattice. Details of their crystalline structure and symmetry may be found in Refs. 47, 49, 60. The calculations were carried out with the Vienna Ab-initio Simulation Package (VASP) [61] using plane-wave basis sets and ultra-soft pseudopotentials [62, 63]. The Ceperly-Alder functional [64] was used to approximate the exchange-correlation term. This method has been extensively and successfully used to study many properties of a variety of types I & II clathrates [17, 47, 49, 60]. In those studies, the calculated properties were in good agreement with experiment. The effects of the generalized gradient approximation (GGA) correction to the LDA were examined by others for the pristine type II Si_{136} material and were found to be minor [47].

The calculations are carried out as follows. First, using VASP, we optimize the geometry of each compound by choosing a fixed volume of the face centered cubic unit cell and relaxing the internal coordinates of the atoms through a conjugate gradient algorithm using atomic forces. The process is repeated for several different unit cell volumes until the global minimum energy is found. Brillouin zone integrations were performed using a $4 \times 4 \times 4$ Monkhorst-Pack k -point grid [65], with a cutoff energy of 300 eV. The accuracy of the total energy convergence was set at 10^{-7} eV. Once the

equilibrium lattice geometry is obtained for each material, the resulting LDA energy versus volume curve is fit with the Birch-Murnaghan equation of state (EOS) [53],

$$E(V) = E_0 + \frac{9}{8} K V_0 \left[\left(\frac{V_0}{V} \right)^{2/3} - 1 \right]^2 \left\{ 1 + \left(\frac{4 - K'}{2} \right) \left[1 - \left(\frac{V_0}{V} \right)^{2/3} \right] \right\} \quad (4.1)$$

where, E and E_0 are the energy and the minimum energy, V and V_0 are the volume and the volume at the minimum energy, K and K' are the bulk modulus and its pressure derivative. This fitting determines the minimum binding energy E_0 , the corresponding volume V_0 , the equilibrium bulk modulus K and its pressure derivative $K' = dK/dP$. Then, using VASP, the electronic band structures and densities of states are calculated for the optimized geometry by generating a separate set of k -points along certain high symmetry directions in the Brillouin zone.

The vibrational dispersion relations are calculated by obtaining the dynamical matrix. The first step is to obtain the force constant matrix by moving each atom by a small finite displacement U_0 (0.02 Å). The total energy for a large supercell with small displacements of the atoms from their equilibrium positions is given by,

$$E_{tot} = E_0 + \frac{1}{2} \sum_{\alpha, i} \sum_{\beta, j} \varphi_{\alpha\beta}^{ij} U_{\alpha}^i U_{\beta}^j, \quad \alpha, \beta = 1, 2, \dots, N \text{ and } i, j = x, y, z \text{ directions.} \quad (4.2)$$

E_0 is the static lattice energy and N is the total number of atoms. U_{α}^i is the displacement of the atom α in the i th direction, and similarly for U_{β}^j . VASP [61] allows the determination of the force constant matrix by calculating the Hessian matrix (matrix obtained from the second derivatives of energy with respect to the atomic positions). The direct space force constant matrix is then given by,

$$\varphi_{\alpha\beta} = \frac{\partial^2 E}{\partial x_{\alpha} \partial x_{\beta}}. \quad (4.3)$$

A complete row of the force constant matrix is obtained for each move. Each atom is moved by $\pm U_0$ and the average value of the force constant is obtained from the second derivative of the energy. The force constant matrix thus obtained is for wave vector $\vec{q} = (0,0,0)$.

A $2 \times 2 \times 2$ k -point grid and 150 eV cutoff energy has been used to calculate the Γ -point phonon modes. Calculations repeated with a $4 \times 4 \times 4$ k -point grid did not result in any appreciable difference in the frequencies.

In order to obtain the dynamical matrix at non-zero \vec{q} , we introduce an approximation which assumes that the force constant matrix elements vanishes for atoms that are separated by a distance that are greater than the third nearest neighbor. Details of this method may be found in Refs. 47, 49. Using this approximation, the dynamical matrix at any \vec{q} is given by,

$$D_{\alpha\beta}(\vec{q}) = \sum \frac{\phi_{\alpha\beta}}{\sqrt{m_\alpha m_\beta}} \exp\left[-\vec{q} \cdot (\vec{R}_\beta - \vec{R}_\alpha)\right] \quad (4.4)$$

where, \vec{q} is the wave-vector in the Brillouin zone and \vec{R} are the position vectors of the nearest neighbor atoms. Once the dynamical matrix is constructed, its diagonalization gives the eigenvalues (squared frequencies) and eigenvectors. The vibrational frequencies (ω) are obtained by solving the equation,

$$|D_{\alpha\beta}(\vec{q}) - \omega^2 \delta_{\alpha\beta}| = 0 . \quad (4.5)$$

The thermodynamic properties are evaluated by calculating the Helmholtz free energy. In the harmonic approximation, the vibrational contribution to the Helmholtz free energy is given by [66],

$$F_{vib}(T) = k_B T \int_0^\infty \left[\frac{1}{2} \hbar \omega + k_B T \ln(1 - e^{-\hbar \omega / k_B T}) \right] g(\omega) d\omega \quad (4.6)$$

where, k_B is the Boltzmann constant, h is the Planck constant and $g(\omega)$ is the vibrational density of states (VDos). $g(\omega)$ is normalized such that $\int g(\omega) d\omega = 3N$, N being the number of atoms. The vibrational entropy is given by,

$$S = - \left(\frac{\partial F_{vib}}{\partial T} \right)_V = k_B \int_0^\infty \left[\frac{\hbar \omega}{k_B T} (e^{\hbar \omega / k_B T} - 1)^{-1} - \ln(1 - e^{-\hbar \omega / k_B T}) \right] g(\omega) d\omega . \quad (4.7)$$

The specific heat capacity at constant volume is calculated using,

$$C_V = -T \left(\frac{\partial^2 F_{vib}}{\partial^2 T} \right)_V = T \left(\frac{\partial S}{\partial T} \right)_V . \quad (4.8)$$

CHAPTER V
STRUCTURAL AND ELECTRONIC
PROPERTIES

After the structural optimization, the total LDA energies at various volumes were fitted to the Birch-Murnaghan equation of state [60], as described in the previous chapter. The results for the fitting parameters E_0 , V_0 , K , K' and the total binding energy per fcc unit cell are listed in Table 5.1 for the different Si clathrates. Experimental values of some of the parameters for Si_{136} are also listed [67, 68]. As expected, the predicted total binding energy per fcc unit cell for the completely and partially filled clathrates is higher than that for the guest-free Si_{136} .

Table 5.1: Birch-Murnaghan equation of state parameters ($T = 0$ K) obtained from a fit of the LDA energy versus volume curve for $\text{Na}_{16}\text{Rb}_8\text{Si}_{136}$, $\text{K}_{16}\text{Rb}_8\text{Si}_{136}$, $\text{Rb}_8\text{Ga}_8\text{Si}_{128}$, $\text{Cs}_8\text{Ga}_8\text{Si}_{128}$ and Si_{136} . Also listed are the available experimental parameters for Si_{136} obtained at $T = 298$ K [67, 68].

Clathrate	E_0 (eV/atom)	V_0 ($\text{\AA}^3/\text{atom}$)	K (GPa)	K'
$\text{Na}_{16}\text{Rb}_8\text{Si}_{136}$	-5.34	19.59	81.88	1.79
$\text{K}_{16}\text{Rb}_8\text{Si}_{136}$	-5.33	19.78	86.17	0.51
$\text{Rb}_8\text{Ga}_8\text{Si}_{128}$	-5.56	21.76	81.26	0.23
$\text{Cs}_8\text{Ga}_8\text{Si}_{128}$	-5.61	21.45	80.33	4.42
Si_{136}	-5.87	22.71	83.23	3.58
Expt. Si_{136}	-	23.01	90	5.2

Table 5.2 shows the calculated and experimental values of the lattice constants for Si_{136} and $\text{Na}_{16}\text{Rb}_8\text{Si}_{136}$ [25, 29]. It also shows the calculated values for $\text{K}_{16}\text{Rb}_8\text{Si}_{136}$, $\text{Rb}_8\text{Ga}_8\text{Si}_{128}$ and $\text{Cs}_8\text{Ga}_8\text{Si}_{128}$. The equilibrium volume for $\text{Na}_{16}\text{Rb}_8\text{Si}_{136}$ gives a cubic lattice

constant of 14.63 Å, about 0.7% smaller than the experimental value of 14.738 Å [29]. The slightly higher value of the lattice constant of the filled clathrates compared to that of Si₁₃₆ (14.56 Å), indicates that the framework structure expands upon inclusion of the guest atoms. However, the calculated lattice constant of Cs₈Ga₈Si₁₂₈ remains same as that of Si₁₃₆. We speculate that this may be due to the local density approximation. Even though the Cs atom is larger than Rb, the LDA does not reflect the expansion of the Cs containing cages [60].

Table 5.2: Calculated and available experimental values of the lattice constants for Na₁₆Rb₈Si₁₃₆, K₁₆Rb₈Si₁₃₆, Rb₈Ga₈Si₁₂₈, Cs₈Ga₈Si₁₂₈ and Si₁₃₆ clathrates [30, 34].

Clathrate	Calculated (Å)	Experiment (Å)
Na ₁₆ Rb ₈ Si ₁₃₆	14.63	14.738
K ₁₆ Rb ₈ Si ₁₃₆	14.64	-
Rb ₈ Ga ₈ Si ₁₂₈	14.63	-
Cs ₈ Ga ₈ Si ₁₂₈	14.56	-
Si ₁₃₆	14.56	14.626

Experimentally it is seen that in the completely filled clathrates the smaller atoms preferentially occupy the smaller cages (dodecahedra) while the larger atoms occupy the slightly larger cages (hexacaidecahedra) [69, 70]. In Na₁₆Rb₈Si₁₃₆ and K₁₆Rb₈Si₁₃₆ the smaller Na and K atoms occupy the dodecahedra and the larger Rb and Cs atoms are located inside the hexacaidecahedra cages. The Rb and Cs atoms in Rb₈Ga₈Si₁₂₈ and Cs₈Ga₈Si₁₂₈ are located inside the large cages.

Table 5.3 shows the calculated and available experimental values of the lattice constants of Ge₁₃₆, Na₁₆Rb₈Ge₁₃₆ and Na₁₆Cs₈Ge₁₃₆ [43, 44, 69]. As seen from Table 5.3,

the experimental lattice constants of Ge_{136} and $\text{Na}_{16}\text{Cs}_8\text{Ge}_{136}$ are almost same. This may be due to the omni-presence of small amounts of alkali metals in the experiments for Ge_{136} which may expand the lattice slightly. This may also be the reason for the difference between the LDA calculated and the experimental lattice constant of Ge_{136} .

Table 5.3: Calculated and available experimental values of the lattice constants for Ge_{136} , $\text{Na}_{16}\text{Rb}_8\text{Ge}_{136}$ and $\text{Na}_{16}\text{Cs}_8\text{Ge}_{136}$ clathrates [43, 44, 69].

Clathrate	Calculated (\AA)	Experiment (\AA)
Ge_{136}	15.11	15.48
$\text{Na}_{16}\text{Rb}_8\text{Ge}_{136}$	15.35	-
$\text{Na}_{16}\text{Cs}_8\text{Ge}_{136}$	15.44	15.4805

The predicted results for E_0 , V_0 , K and K' for Ge_{136} , $\text{Na}_{16}\text{Rb}_8\text{Ge}_{136}$ and $\text{Na}_{16}\text{Cs}_8\text{Ge}_{136}$ are listed in Table 5.4. In $\text{Na}_{16}\text{Rb}_8\text{Ge}_{136}$ and $\text{Na}_{16}\text{Cs}_8\text{Ge}_{136}$ the Na atoms are inside the dodecahedra and the Rb and Cs atoms are inside the hexacaidecahedra cages.

Table 5.4: The parameters of the Birch-Murnaghan equation of state obtained from a fit of the LDA energy versus volume curve for Ge_{136} , $\text{Na}_{16}\text{Rb}_8\text{Ge}_{136}$ and $\text{Na}_{16}\text{Cs}_8\text{Ge}_{136}$.

Clathrate	E_0 (eV/atom)	V_0 ($\text{\AA}^3/\text{atom}$)	K (GPa)	K'
Ge_{136}	-5.127	25.49	61.27	4.67
$\text{Na}_{16}\text{Rb}_8\text{Ge}_{136}$	-4.682	22.68	49.36	5.8
$\text{Na}_{16}\text{Cs}_8\text{Ge}_{136}$	-4.683	22.95	48.01	3.6

Figure 5.1(a, b) shows the energy versus volume curve for the different Si and Ge clathrates. Although the energy per atom is slightly less for the filled clathrates as seen in Fig. 5.1, the total binding energy per fcc unit cell is higher for the filled clathrates (see

Table 5.1). This is because there are 40 atoms/fcc unit cell for the completely filled clathrates compared to the 34 atoms/fcc unit cell in the pristine Si_{136} or Ge_{136} .

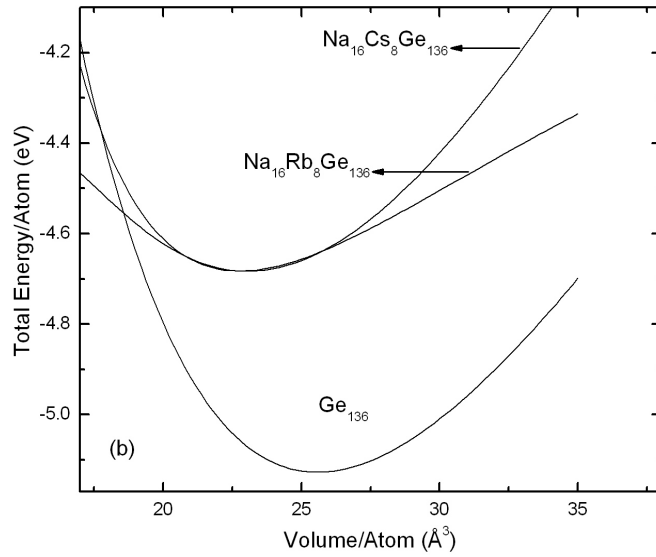
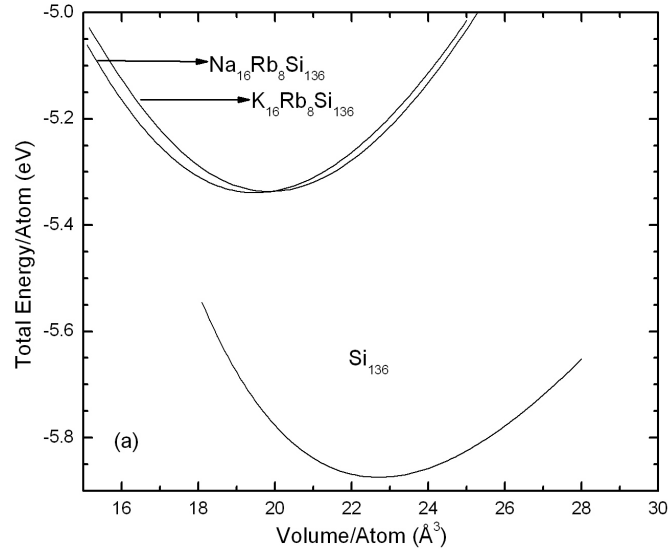
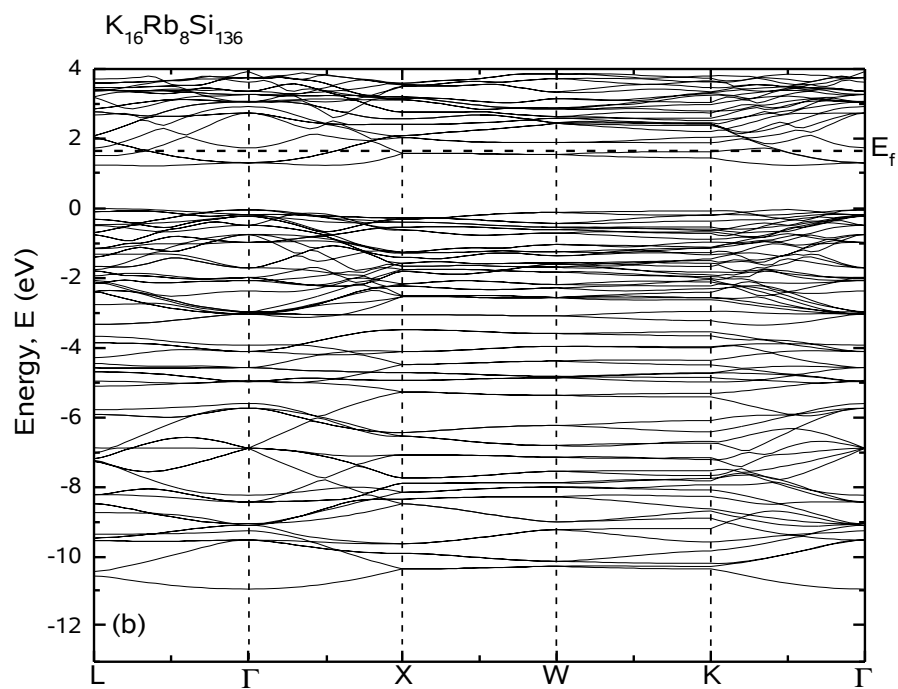
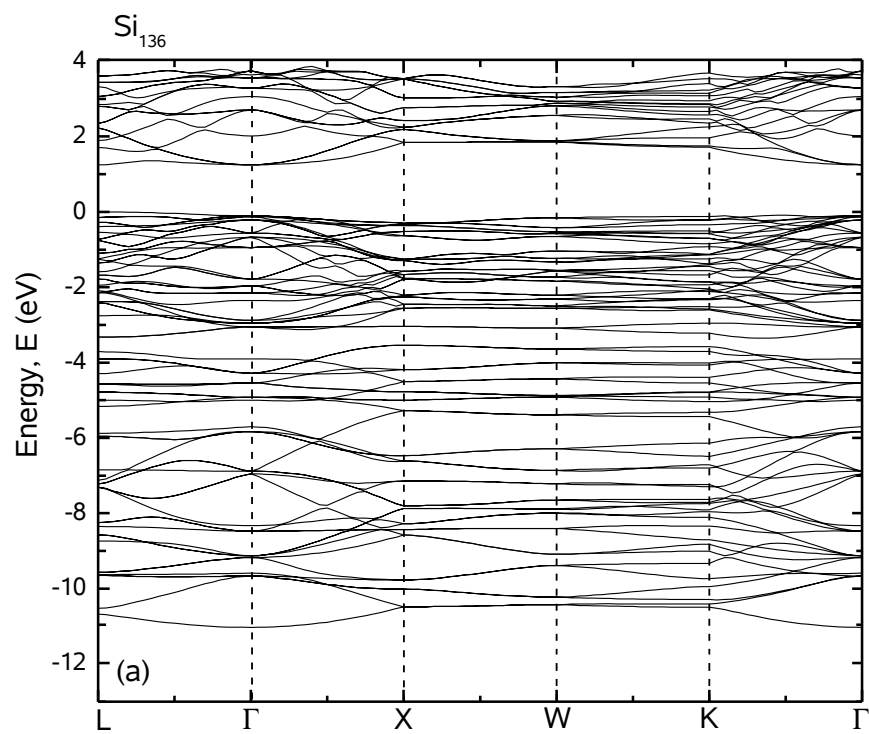


Figure 5.1: Equation of state (E vs. V) of (a) Si_{136} , $\text{Na}_{16}\text{Rb}_8\text{Si}_{136}$ and $\text{K}_{16}\text{Rb}_8\text{Si}_{136}$ and (b) Ge_{136} , $\text{Na}_{16}\text{Rb}_8\text{Ge}_{136}$ and $\text{Na}_{16}\text{Cs}_8\text{Ge}_{136}$.

The electronic band structure and density of states (DOS) calculations were done for the clathrates at their optimized geometries. It is well-known that the LDA underestimates the minimum energy band gaps. However, it has been shown to predict energy differences and trends correctly, so a comparison of the band gaps between clathrates should be meaningful. Figure 5.2(a, b, c) shows the predicted electronic band structures for Si_{136} , $\text{K}_{16}\text{Rb}_8\text{Si}_{136}$ and $\text{Na}_{16}\text{Rb}_8\text{Si}_{136}$, respectively. To enable an easy qualitative comparison, for each material we have chosen the zero of energy at the top of the valence band.

The gap between the highest filled (valence band top) and the lowest empty band (bottom of conduction band) is estimated as the band gap. The pristine material, Si_{136} , has a predicted indirect band gap of about 1.24 eV, in agreement with LDA results obtained by others [47]. The band structure results for $\text{Na}_{16}\text{Rb}_8\text{Si}_{136}$ and $\text{K}_{16}\text{Rb}_8\text{Si}_{136}$ are nearly identical to those of the parent Si_{136} clathrate.

Since all host framework bonds are satisfied by the Si valence electrons, electrons from the guests occupy the conduction states of the parent Si_{136} . The Fermi levels for the filled clathrates lie within the Si_{136} conduction band, as shown in Figs. 5.2(b, c). Our results agree qualitatively with the “rigid-band model” [71], which predicts that the bands for the guest-containing materials are nearly the same as those of the framework and that there is a charge transfer from the guests into the host conduction states. This raises the Fermi level (E_f) into the conduction band. The band structure results for $\text{Na}_{16}\text{Rb}_8\text{Si}_{136}$ are consistent with the metallic behavior reported for that material by Lattner et al [29].



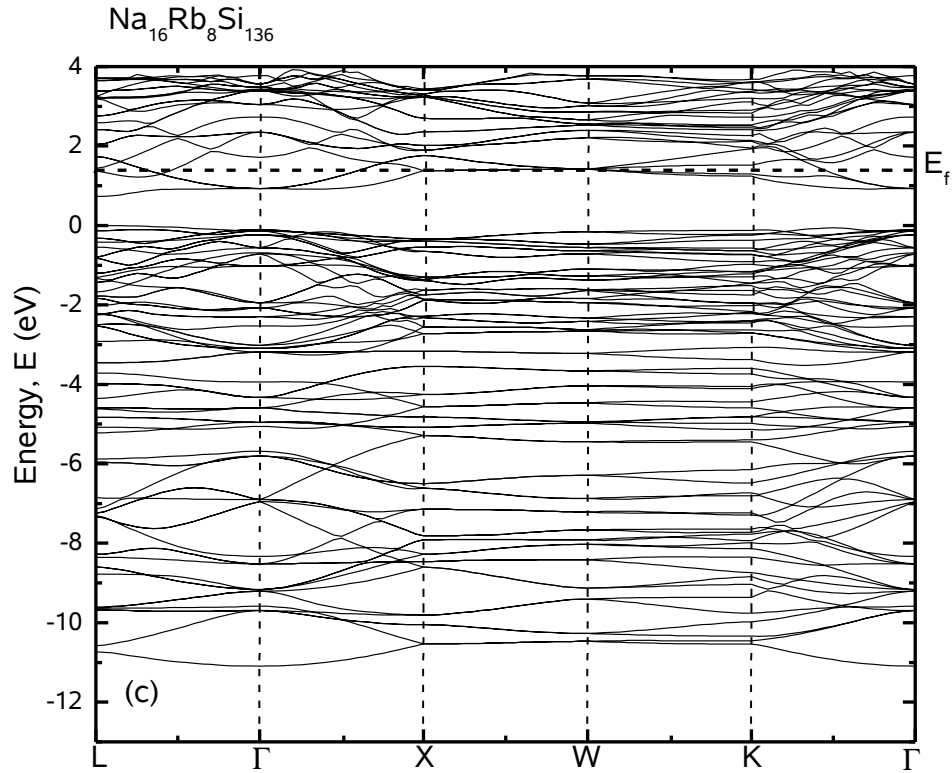


Figure 5.2: Electronic band structures of (a) Si_{136} (b) $\text{K}_{16}\text{Rb}_8\text{Si}_{136}$ and (c) $\text{Na}_{16}\text{Rb}_8\text{Si}_{136}$. In all figures, the top of the valence band is the zero of energy. In Figs. (b) and (c), the Fermi level is pushed into the conduction band as shown by a dashed line at ~ 1.6 and 1.4 eV, respectively.

Figure 5.3 shows the predicted total electronic density of states (DOS) for the Si_{136} , $\text{K}_{16}\text{Rb}_8\text{Si}_{136}$ and $\text{Na}_{16}\text{Rb}_8\text{Si}_{136}$ clathrates. The DOS distribution near the Fermi level of the filled clathrates show a charge transfer from the different guest atoms to the Si framework. The DOS near the Fermi level is higher for these filled clathrates, because the guest atoms donate electrons to the Si framework. This increase might be associated with the metallic behavior observed in $\text{Na}_{16}\text{Rb}_8\text{Si}_{136}$ [29].

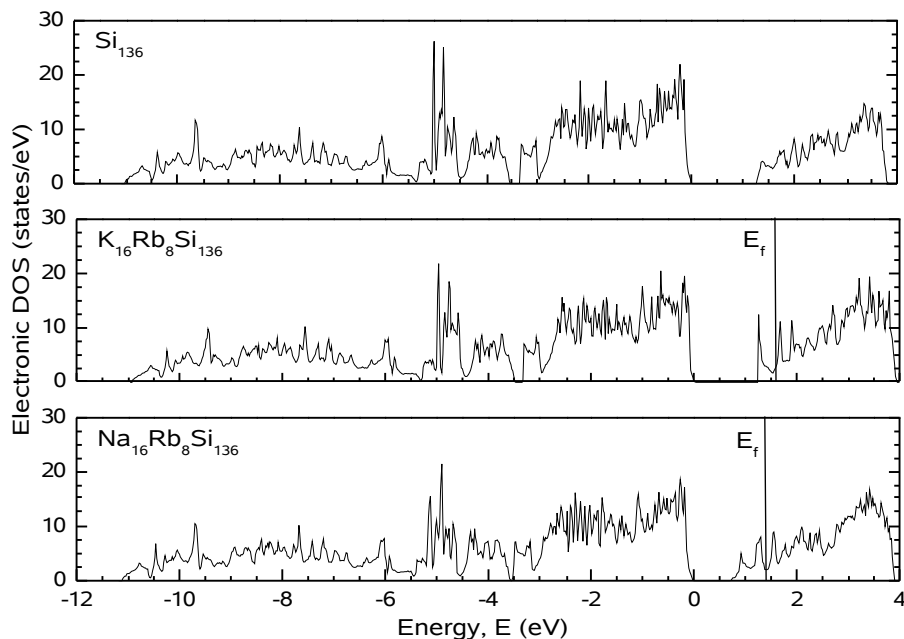


Figure 5.3: Electronic density of states of Si_{136} , $\text{K}_{16}\text{Rb}_8\text{Si}_{136}$ and $\text{Na}_{16}\text{Rb}_8\text{Si}_{136}$ in the valence band and the lower portion of the conduction band. The Fermi levels of $\text{K}_{16}\text{Rb}_8\text{Si}_{136}$ and $\text{Na}_{16}\text{Rb}_8\text{Si}_{136}$ are shown by a vertical line.

Figure 5.4 shows the predicted electronic band structures of $\text{Rb}_8\text{Ga}_8\text{Si}_{128}$ and $\text{Cs}_8\text{Ga}_8\text{Si}_{128}$, respectively. The Si_{136} framework has three Wyckoff sites, viz. $8a$, $32e$ and $96g$. The eight Ga atoms are substituted at the $8a$ crystallographic sites of the Si-framework. This ensures an energetically favored configuration with no Ga – Ga bond. Similar substitution made at the “ e ” or “ g ” sites resulted in higher total energies. The band structures again can be qualitatively described in the context of the rigid-band model. This rigid band character of the band structure means that the guest to framework interactions are predominantly ionic in nature and that the guest atoms act as electron donors. It also indicates that the Ga atoms in the framework, with their s^2p^1 valence electronic configuration, allow the covalent Ga – Si bonds to accept electrons from the guest atoms.

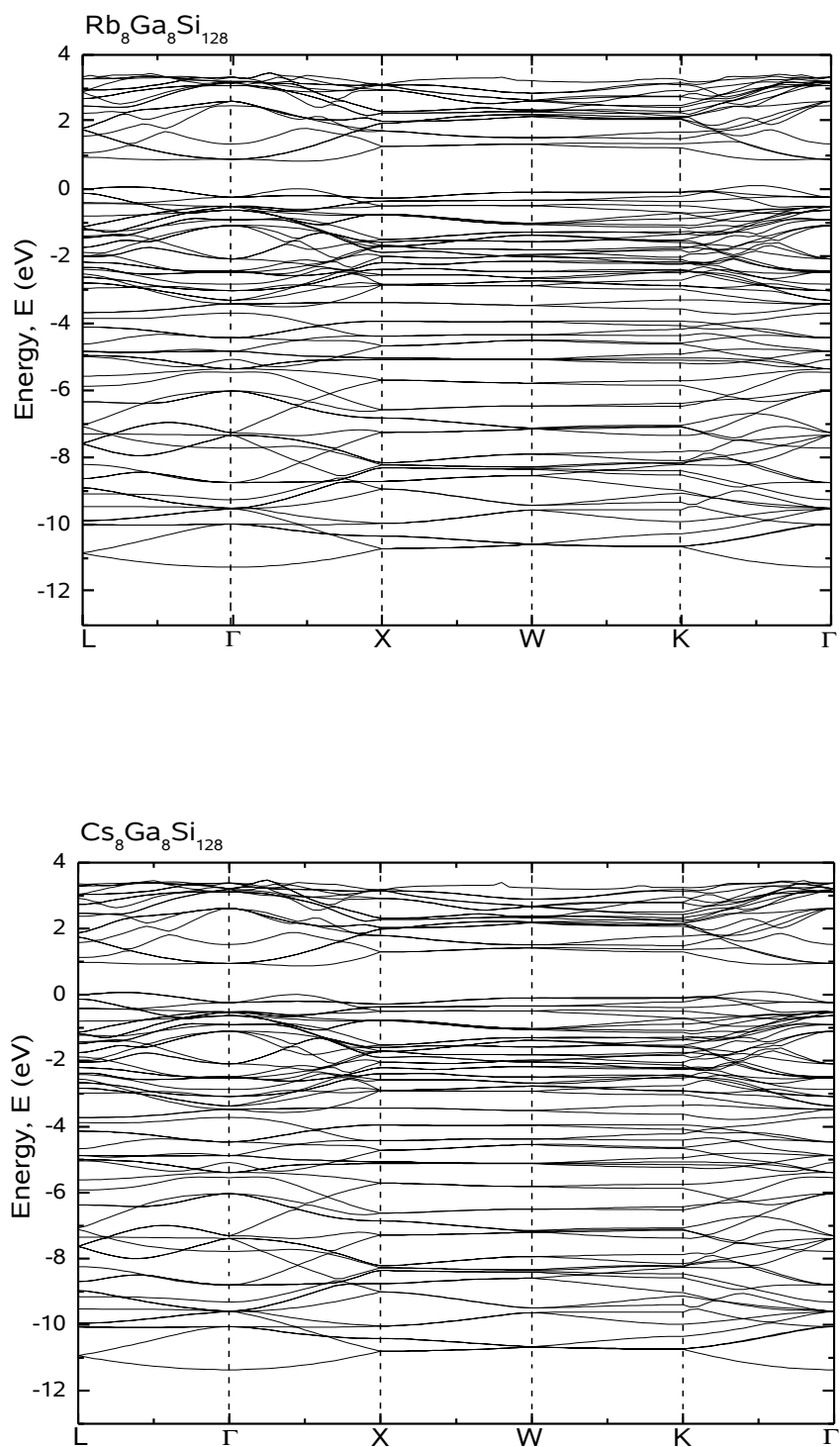


Figure 5.4: Electronic band structures of $\text{Rb}_8\text{Ga}_8\text{Si}_{128}$ and $\text{Cs}_8\text{Ga}_8\text{Si}_{128}$. The top of the valence band is taken as the zero of energy. In $\text{Rb}_8\text{Ga}_8\text{Si}_{128}$ and $\text{Cs}_8\text{Ga}_8\text{Si}_{128}$ there is an indirect band gap of ~ 0.73 and 0.77 eV, respectively.

The band structure calculations show that $\text{Rb}_8\text{Ga}_8\text{Si}_{128}$ and $\text{Cs}_8\text{Ga}_8\text{Si}_{128}$ are semiconducting with predicted indirect band gaps of approximately 0.73 and 0.77 eV, respectively. This is in contrast to the predicted band structure for $\text{Rb}_8\text{Si}_{136}$ (not shown) and $\text{Na}_{16}\text{Rb}_8\text{Si}_{136}$, which were found to be metallic in character. The reason for this is that all host Si – Si bonds in $\text{Rb}_8\text{Si}_{136}$ and $\text{Na}_{16}\text{Rb}_8\text{Si}_{136}$ are satisfied by the Si valence electrons. Therefore in those materials, electrons from the guest atoms occupy the host conduction band states, making the materials metallic. This is not the case in $\text{Rb}_8\text{Ga}_8\text{Si}_{128}$ and $\text{Cs}_8\text{Ga}_8\text{Si}_{128}$, due to the unpaired p electrons in the Ga atoms.

In order to emphasize the effect of Ga substitution, we have included in Fig. 5.5 the total electronic density of states (DOS) of $\text{Rb}_8\text{Si}_{136}$ along with those of $\text{Rb}_8\text{Ga}_8\text{Si}_{128}$ and $\text{Cs}_8\text{Ga}_8\text{Si}_{128}$. For each material we have chosen the zero of energy at the top of the valence band. Unlike the Ga-substituted clathrates, the Fermi level (E_f) of $\text{Rb}_8\text{Si}_{136}$ was found to lie inside the conduction band. $\text{Rb}_8\text{Si}_{136}$ is predicted to have a metallic property.

Figure 5.6 shows the s and p -orbital projected density of states for the guest Rb and substitutional Ga atoms in $\text{Rb}_8\text{Ga}_8\text{Si}_{128}$. It shows the Ga p -states near the top of the valence band which are likely responsible for the semiconducting nature of this material. The gap between the valence and conduction bands is considerably reduced in the filled clathrates, when compared to the calculated LDA band gap of about 1.24 eV in pristine Si_{136} . Figure 5.6 shows the Ga p -states at the top of the valence band and the Rb s -states near the bottom of the conduction band. These states are likely the cause for the reduction in the overall gap between the valence and conduction bands in the filled clathrates.

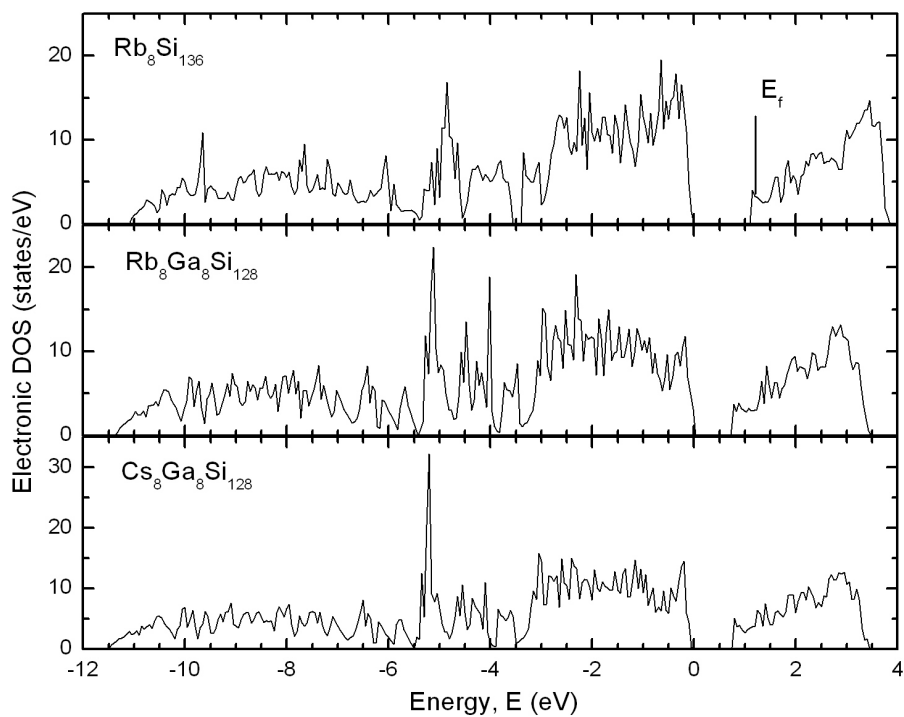


Figure 5.5: Total electronic density of states of $\text{Rb}_8\text{Si}_{136}$, $\text{Rb}_8\text{Ga}_8\text{Si}_{128}$ and $\text{Cs}_8\text{Ga}_8\text{Si}_{128}$. The Fermi level of $\text{Rb}_8\text{Si}_{136}$ lies at the bottom of the conduction band as shown by a vertical line.

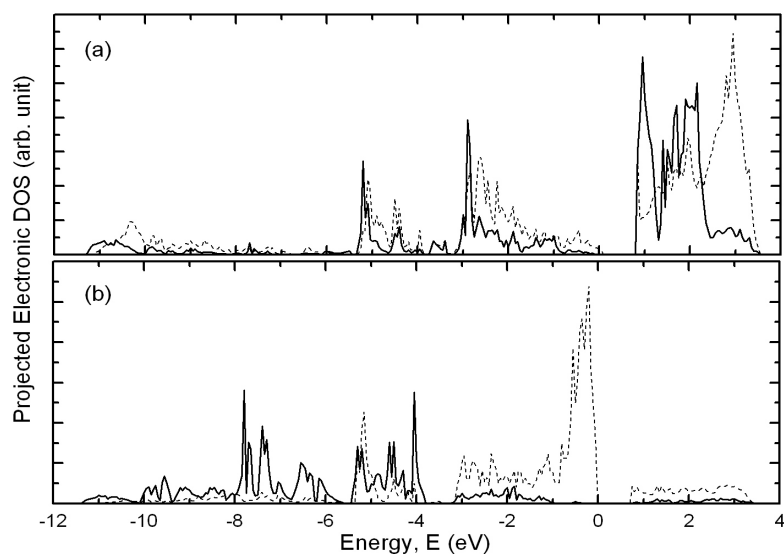


Figure 5.6: *s* (solid curve) and *p*-orbital (dashed curve) projected density of states for (a) Rb and (b) Ga atoms in $\text{Rb}_8\text{Ga}_8\text{Si}_{128}$.

Experimentally measured total thermal conductivity of the filled type II clathrates is higher compared to those of the type I structure [30]. This is because of their metallic character, which increases the electronic contribution to the total thermal conductivity. The semiconducting nature of $\text{Rb}_8\text{Ga}_8\text{Si}_{128}$ and $\text{Cs}_8\text{Ga}_8\text{Si}_{128}$ may help reduce this electronic contribution.

Figure 5.7 shows the predicted electronic band structure for Ge_{136} . The LDA band gap for Ge_{136} is approximately 0.75 eV, similar to the band gap found in other studies [49]. Figure 5.8 shows the predicted electronic band structures for $\text{Na}_{16}\text{Rb}_8\text{Ge}_{136}$ and $\text{Na}_{16}\text{Cs}_8\text{Ge}_{136}$, respectively.

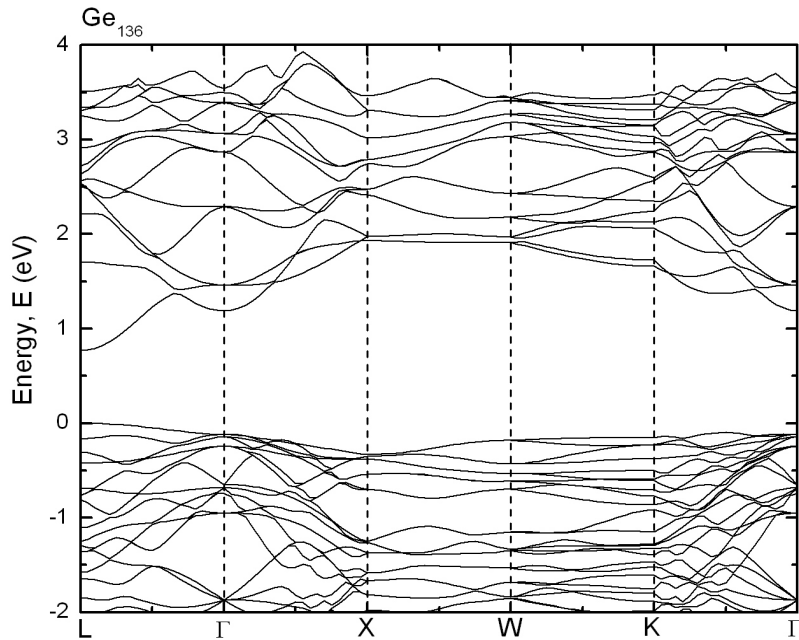


Figure 5.7: Electronic band structure of Ge_{136} .

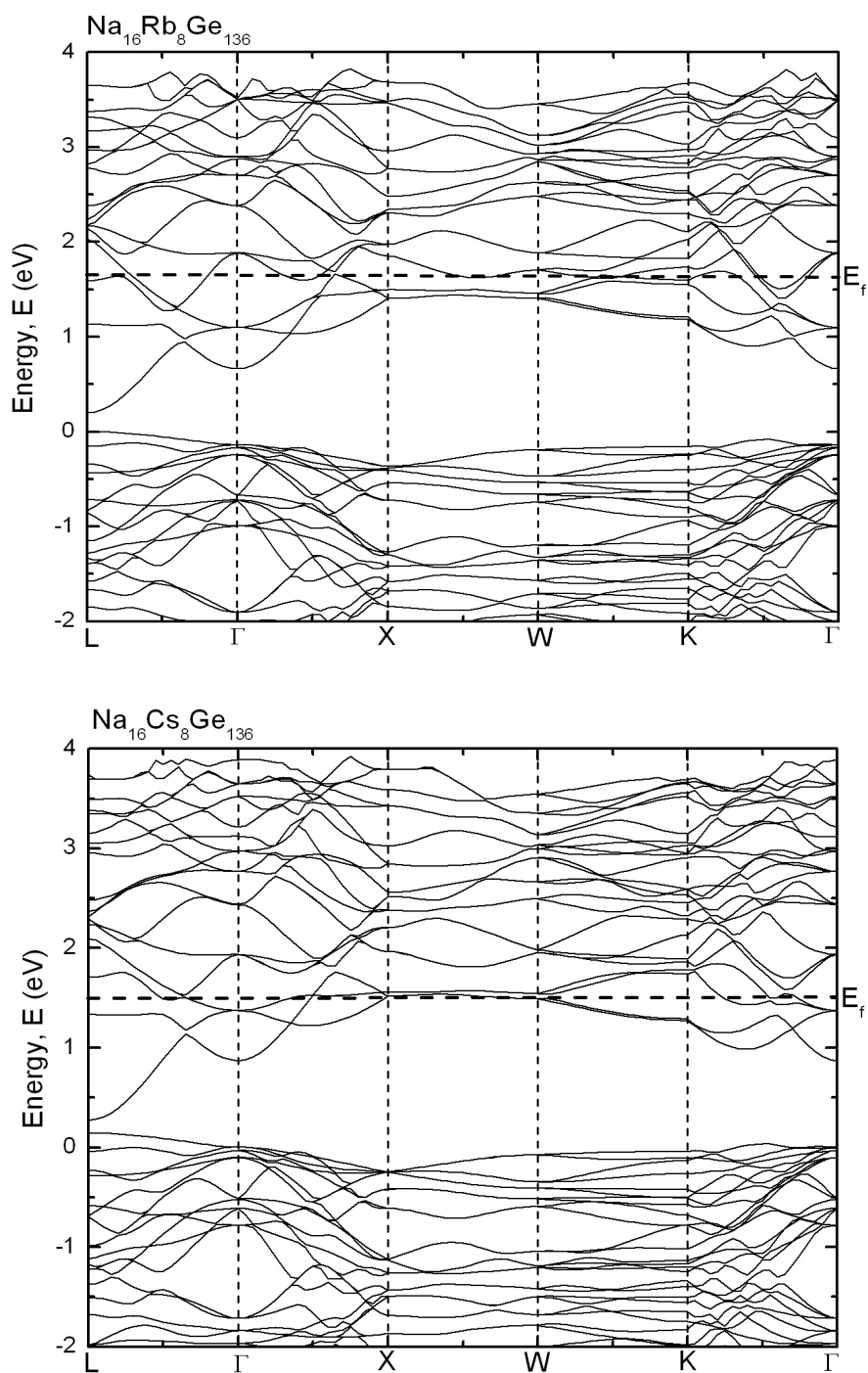


Figure 5.8: Electronic band structures of $\text{Na}_{16}\text{Rb}_8\text{Ge}_{136}$ and $\text{Na}_{16}\text{Cs}_8\text{Ge}_{136}$. In both materials the Fermi level lies inside the conduction band as shown by a dashed line at ~ 1.6 and 1.5 eV, respectively.

As in the case of the Si clathrates, the “rigid-band model” may be applied to the filled Ge clathrates as well. The rigid-band character indicates a charge transfer from the alkali guest atoms to the Ge framework, without any strong hybridization of the states near the Fermi level. $\text{Na}_{16}\text{Rb}_8\text{Ge}_{136}$ and $\text{Na}_{16}\text{Cs}_8\text{Ge}_{136}$ are predicted to be metallic which is consistent with experimental observations [69, 70].

Figure 5.9 shows the predicted electronic density of states (DOS) for the different Ge clathrates. The DOS near the Fermi level is higher for both of the filled Ge clathrates, because the guest atoms donate electrons to the Ge framework. This increase might be associated with the metallic behavior observed in $\text{Na}_{16}\text{Rb}_8\text{Ge}_{136}$ and $\text{Na}_{16}\text{Cs}_8\text{Ge}_{136}$ [69, 70].

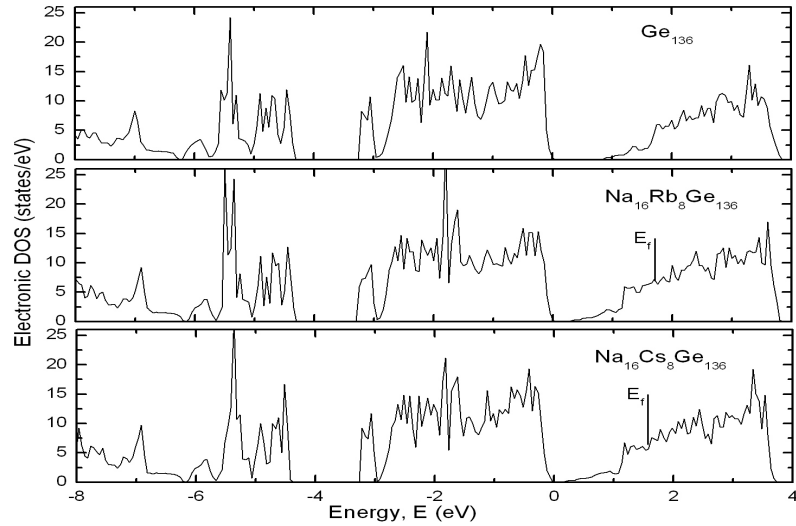


Figure 5.9: Electronic density of states of Ge_{136} , $\text{Na}_{16}\text{Rb}_8\text{Ge}_{136}$ and $\text{Na}_{16}\text{Cs}_8\text{Ge}_{136}$ in the valence band and the lower portion of the conduction band. The Fermi levels of the filled clathrates are shown by a vertical line.

5.1 Knight Shift

The magnetic coupling of the electrons to the nucleus arises from the interaction of the electron magnetic moment with that of the nucleus. The electron magnetic moment originates from the motion of the electrical charges about the nucleus and due to the

electron spin [72]. The coupling caused by the magnetic moment associated with the electron spin gives rise to the so called Knight shifts which are observed in nuclear magnetic resonance (NMR) experiments. Knight shifts are generally observed in metals.

In the absence of an external magnetic field, there is no preferential orientation of the conduction electron spins in metals. Upon application of an external field, the electron spins become polarized which gives rise to an effective field at the site of the nucleus. This effective field causes a shift in the nuclear resonance, known as the Knight shift.

In recent years, several groups reported on the large shifts observed in NMR studies of filled Si and Ge clathrates [29, 52, 54, 73]. For example, the observed shifts for ^{23}Na in $\text{Na}_x\text{Si}_{136}$ ($7 \leq x \leq 9$ and $x \approx 24$) were between 1600 ppm and 2000 ppm [54]. The values of the shifts were referenced to a 1 molar solution of NaCl taken as 0 ppm. The origin of these shifts were due to the interaction between nucleus under observation and the delocalized electrons from the alkali atoms having energies near the Fermi surface. Hence those observed shifts in the nuclear resonance were characterized as “Knight shifts”. Such Knight shifts have also been reported for $\text{Na}_{16}\text{Rb}_8\text{Si}_{136}$, $\text{Na}_{16}\text{Cs}_8\text{Si}_{136}$ and the $\text{Cs}_8\text{Ge}_{136}$ clathrates [29, 71, 73]. In these type II clathrates, the Knight shifts for ^{23}Na , ^{87}Rb , ^{133}Cs and ^{29}Si each increase with decreasing temperature. The temperature dependence were typically observed in the 140 to 500 K range. For example, the temperature dependence of ^{133}Cs shifts in $\text{Cs}_8\text{Ge}_{136}$ ranged from about 7600 ppm at 300 K to about 6500 ppm at 423 K [73]. This strong temperature dependence is very different from the Knight shift observed in metals, where it is approximately temperature independent [74].

The conduction electrons in metals, whose wave functions are generally derived from the atomic s-orbitals, have non-vanishing wave functions at the site of the nucleus

[75]. Thus a temperature-dependent contribution from the magnitude of the s -component wave function at the nucleus ($|\psi_s(0)|$) may be a contributing factor to the temperature-dependent Knight shift observed in the filled clathrates. Here, we show the results of our calculation of the total and the projected electronic DOS for the different filled clathrates, which gives a qualitative description of the temperature dependence of the observed Knight shifts.

As originally proposed by Gryko et al. [54], the temperature dependent Knight shifts may be related to a structural feature of the electronic DOS of the filled clathrates, which is not generally seen in metals. This consists of two sharp peaks near the Fermi level (E_f), separated by an energy difference (ΔE) which is comparable to $k_B T$, where k_B is the Boltzmann constant. They also postulated that the lower of the two peaks are derived from the donated electrons from the alkali atoms inside the clathrate cages. If the separation between those two peaks is of the order of $k_B T$, then that could possibly explain the temperature dependence of the observed Knight shift. Figure 5.10 shows the electronic densities of states near the lower portion of the conduction band of Si_{136} , $\text{Na}_{16}\text{Rb}_8\text{Si}_{136}$ and $\text{K}_{16}\text{Rb}_8\text{Si}_{136}$.

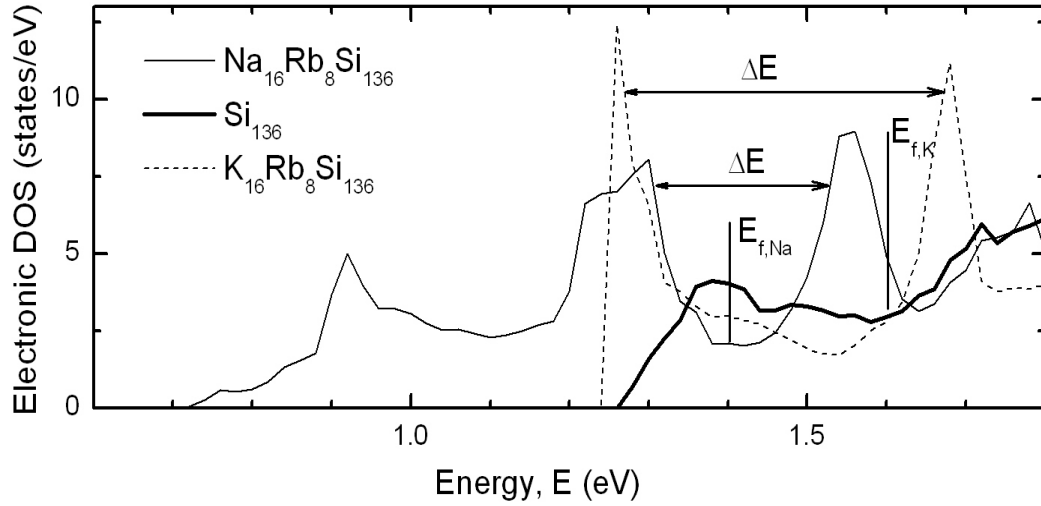


Figure 5.10: Comparison of density of states of Si_{136} , $\text{Na}_{16}\text{Rb}_8\text{Si}_{136}$ and $\text{K}_{16}\text{Rb}_8\text{Si}_{136}$ in the lower portion of the conduction band. Peak separation (ΔE) are shown. Fermi levels for $\text{Na}_{16}\text{Rb}_8\text{Si}_{136}$ and $\text{K}_{16}\text{Rb}_8\text{Si}_{136}$ are shown as $E_{f,\text{Na}}$ and $E_{f,\text{K}}$ respectively.

The above figure shows two peaks, separated by a ΔE near the Fermi level in both $\text{Na}_{16}\text{Rb}_8\text{Si}_{136}$ and $\text{K}_{16}\text{Rb}_8\text{Si}_{136}$. This seems to be consistent with the previous description. However, the ΔE separating the two peaks approximately ranges from 200 to 400 meV (see Fig. 5.10). This is much larger than the $k_B T$ in the range where the observed temperature dependence of the shifts have been reported.

Figure 5.11 shows the lower portion of the conduction band of Ge_{136} , $\text{Na}_{16}\text{Rb}_8\text{Ge}_{136}$ and $\text{Na}_{16}\text{Cs}_8\text{Ge}_{136}$. Interestingly, neither $\text{Na}_{16}\text{Rb}_8\text{Ge}_{136}$ nor $\text{Na}_{16}\text{Cs}_8\text{Ge}_{136}$ show any sharp peaks near their respective Fermi levels. These peak like structures near E_f were not present in band structure calculations of $\text{Cs}_8\text{Ge}_{136}$ either [73]. But $\text{Cs}_8\text{Ge}_{136}$ is known to have a large temperature dependent Knight shift, just like the filled Si clathrates.

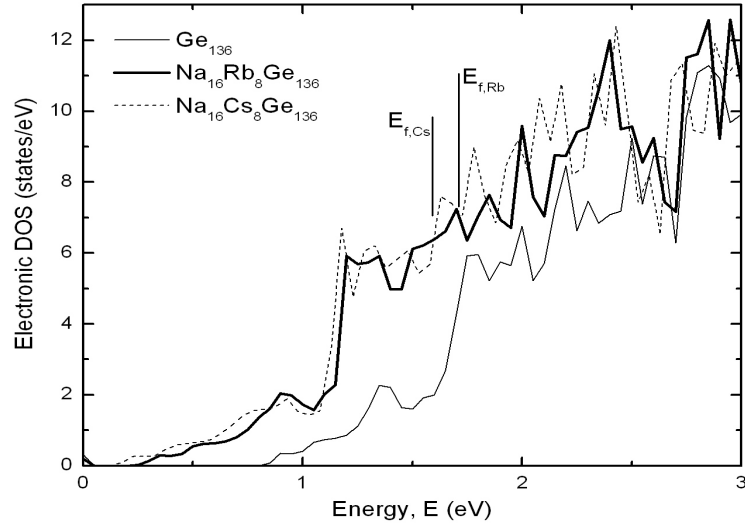


Figure 5.11: Comparison of density of states of Ge_{136} , $\text{Na}_{16}\text{Rb}_8\text{Ge}_{136}$ and $\text{Na}_{16}\text{Cs}_8\text{Ge}_{136}$ in the lower portion of the conduction band. Fermi levels for $\text{Na}_{16}\text{Rb}_8\text{Ge}_{136}$ and $\text{Na}_{16}\text{Cs}_8\text{Ge}_{136}$ are shown as $E_{f,\text{Rb}}$ and $E_{f,\text{Cs}}$ respectively.

Figure 5.12 shows the s and p -orbital projected density of states of the different alkali atoms in the Si clathrates. The wave function character is calculated by projecting the wave functions into spherical harmonics ($Y_{l,m}$), where $l = 0$ corresponds to s -orbitals, $l = 1$ to p -orbitals etc. The projected densities in Fig. 5.12 show the s (solid line) and p -orbital (dashed line) contribution from the Na and the K atoms located in the 20-atom cage, and the Rb inside the 28-atom cage for the Si clathrates.

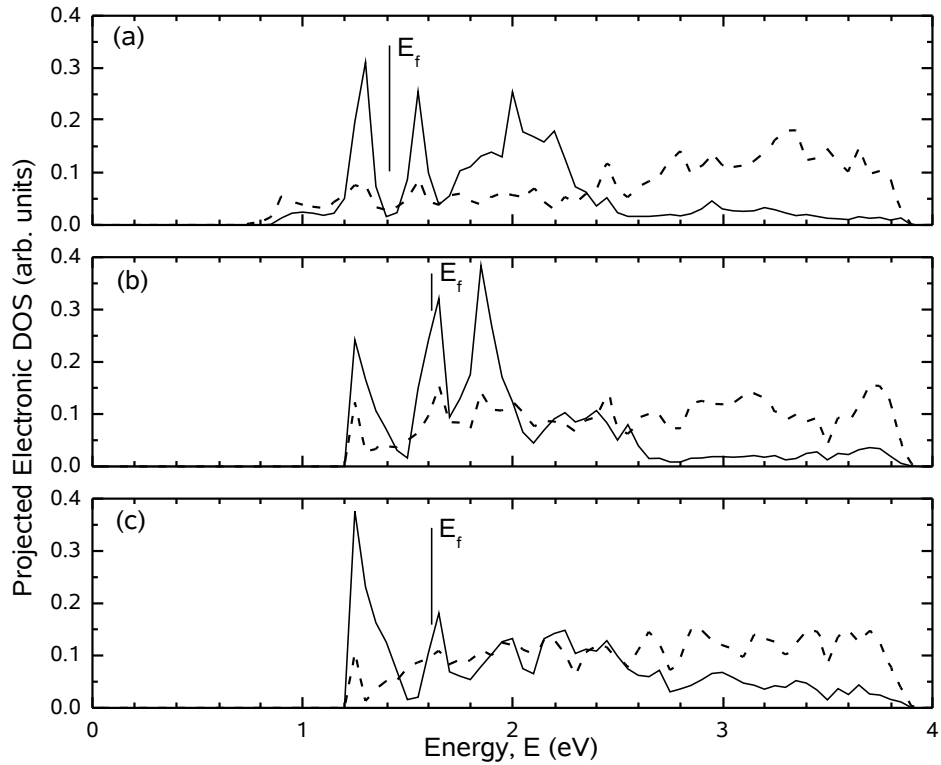


Figure 5.12: s (solid line) and p -orbital (dashed line) projected density of states for (a) Na (b) K and (c) Rb in the lower portion of the conduction band near the Fermi level of the $\text{Na}_{16}\text{Rb}_8\text{Si}_{136}$ and $\text{K}_{16}\text{Rb}_8\text{Si}_{136}$ clathrates.

Figures 5.13 and 5.14 show the calculated projected density of states of the of the Na, Rb and Cs atoms in the $\text{Na}_{16}\text{Rb}_8\text{Ge}_{136}$ and $\text{Na}_{16}\text{Cs}_8\text{Ge}_{136}$ clathrates. The projected densities are shown in the lower part of the conduction band near the Fermi level, E_f . Each of them show the s -orbital character of the states near E_f .

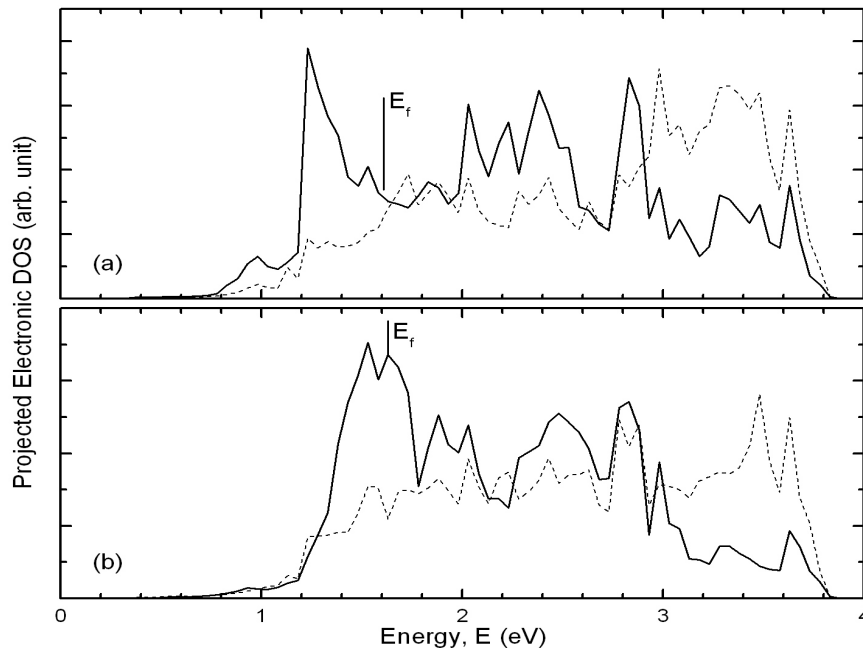


Figure 5.13: s (solid line) and p -orbital (dashed line) projected density of states for (a) Na (b) Rb in the lower portion of the conduction band near the Fermi level of the $\text{Na}_{16}\text{Rb}_8\text{Ge}_{136}$ clathrate.

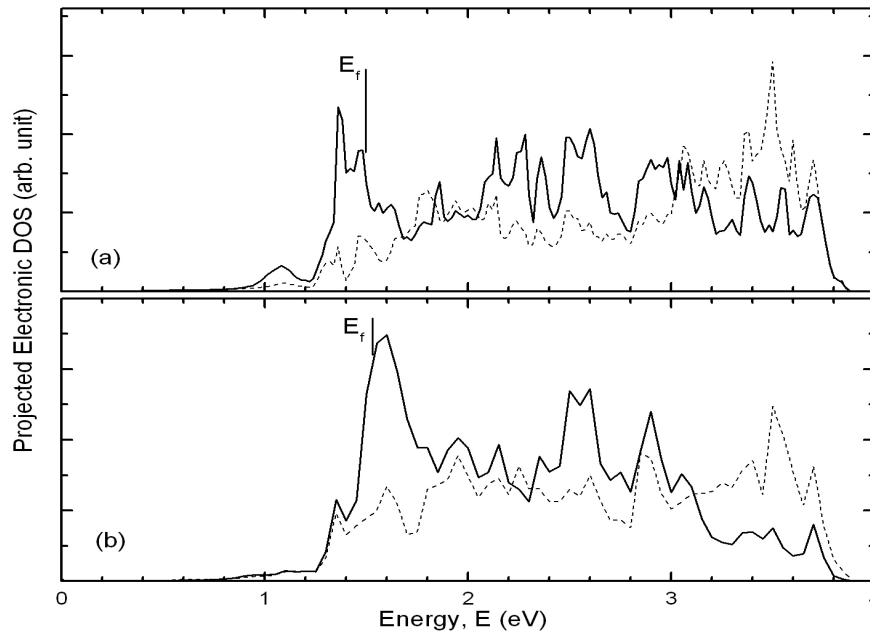


Figure 5.14: s (solid line) and p -orbital (dashed line) projected density of states for (a) Na (b) Cs in the lower portion of the conduction band near the Fermi level of the $\text{Na}_{16}\text{Cs}_8\text{Ge}_{136}$ clathrate.

Based on the calculated projected densities of the different alkali metals in the Si and Ge clathrates, we predict that the states near the Fermi level of the filled clathrates will be similar to an impurity derived donor-like band, irrespective of the presence of sharp peaks near E_f . These donor bands have a more *s*-like character. As one goes higher in energy inside the conduction band, the *s*-like character decreases and the *p*-like character of the states increases. At high temperatures, thermal excitation could promote electrons from the *s*-like alkali states to the *p*-like framework states. This thermal promotion can generally lead to an Arrhenius-like behavior of the susceptibility and Knight shift at higher temperatures. At low temperatures, however, the electrons are more likely to be found in the *s*-like donor bands. As the electrons become more confined to the low-lying donor bands at low temperatures, the magnitude of the *s*-component wave function at the nucleus ($|\psi_s(0)|$) increases, resulting in an increase in the Knight shift.

Unlike metals, which have a broad, featureless DOS at the Fermi level, we predict that these filled clathrates should have a highly structured DOS in that region, meaning a complicated electronic distribution that may vary with changing temperature. Hence, a variation in χ_p , which also depends on the electronic configuration near the Fermi level, is also expected with a temperature variation.

CHAPTER VI
VIBRATIONAL PROPERTIES

Figure 6.1 shows the predicted phonon dispersion curves and the vibrational density of states (VDos) of Si_{136} . The phonon dispersion curves and VDos of $\text{K}_{16}\text{Rb}_8\text{Si}_{136}$ and $\text{Na}_{16}\text{Rb}_8\text{Si}_{136}$ are shown in Fig. 6.2. In Si_{136} , the acoustic phonon modes are located below 100 cm^{-1} and the optical modes lie above 100 cm^{-1} up to approximately 490 cm^{-1} . The experimentally observed highest Γ -phonon frequency in $\text{Na}_1\text{Si}_{136}$ is about 484 cm^{-1} [50] compared to our calculated value of $\sim 490 \text{ cm}^{-1}$ in Si_{136} .

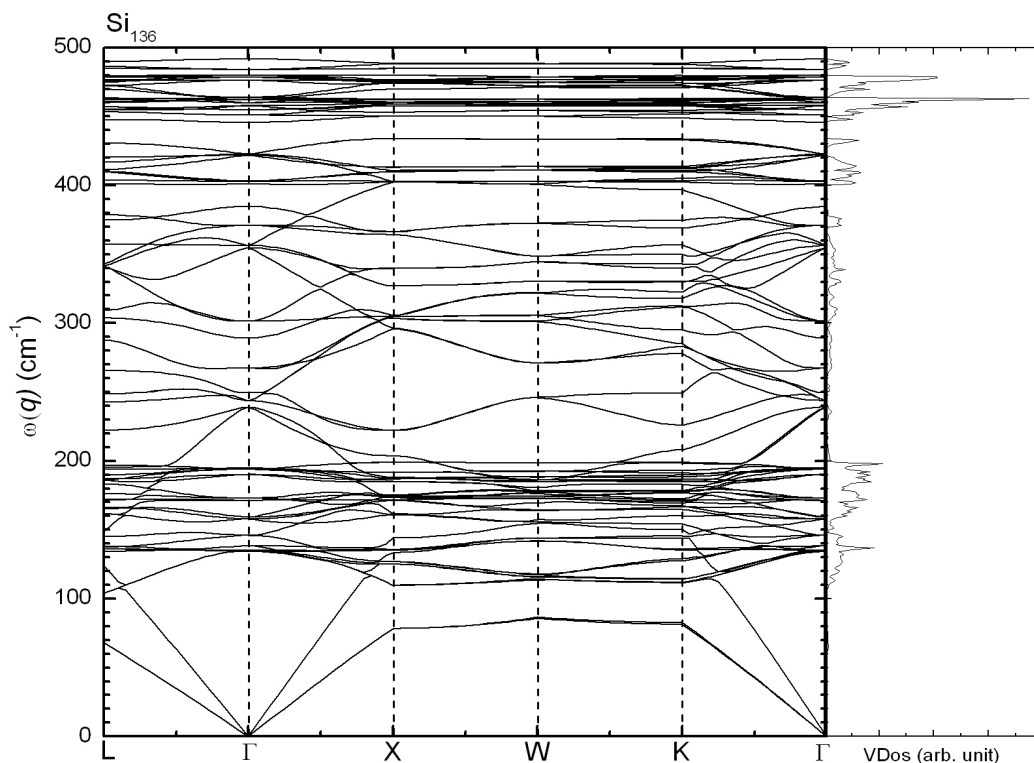


Figure 6.1: Phonon dispersion relations and vibrational density of states (VDos) of Si_{136} .

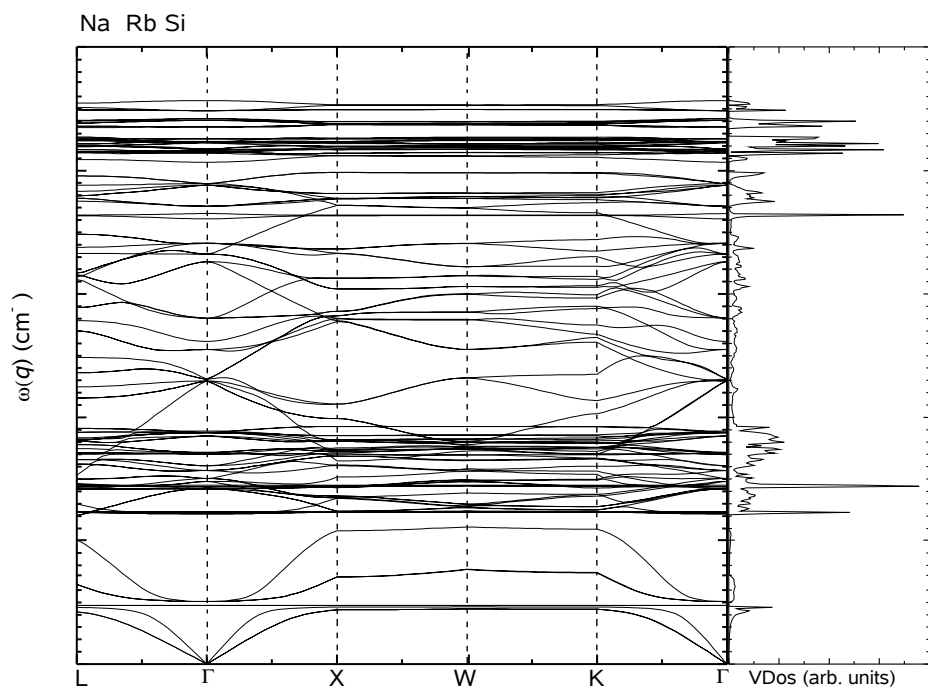
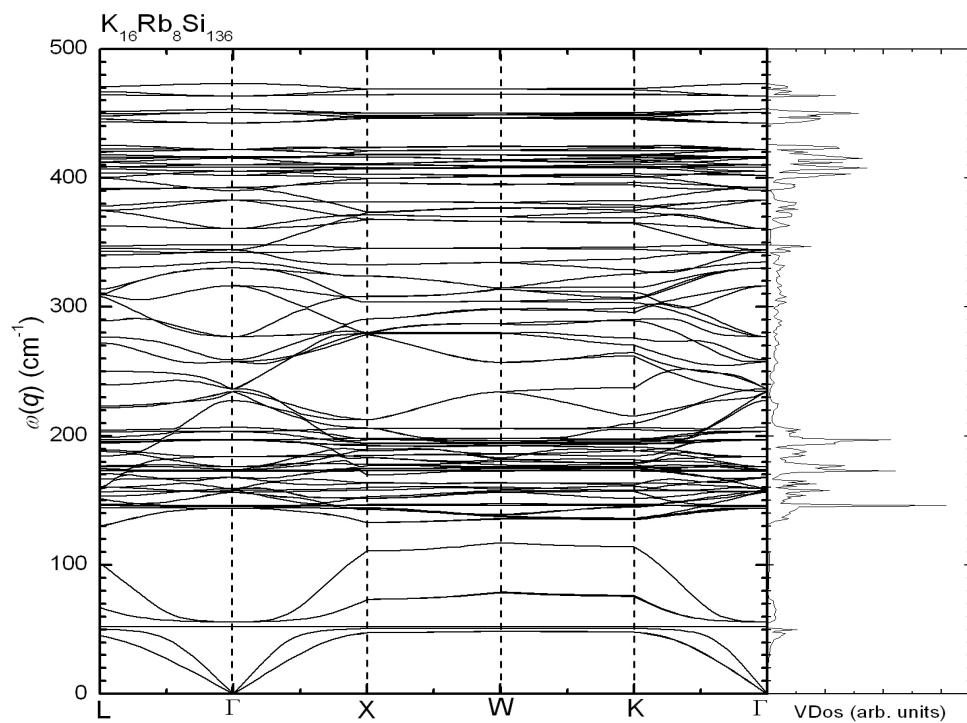


Figure 6.2: Phonon dispersion relations and vibrational density of states (VDos) of $K_{16}Rb_8Si_{136}$ and $Na_{16}Rb_8Si_{136}$.

Figure 6.3 shows the predicted phonon dispersion curves and the VDos of $\text{Rb}_8\text{Ga}_8\text{Si}_{128}$ and $\text{Cs}_8\text{Ga}_8\text{Si}_{128}$, respectively. The phonon dispersion and VDos of $\text{Rb}_8\text{Si}_{136}$ are shown in Fig. 6.4.

Figures 6.2-6.4 are qualitatively similar to each other and they all share some common features. The acoustic modes are located below about 50 cm^{-1} and the optic modes lie above that range. The optical modes are mostly flat, except for a few in the range $200\text{-}280\text{ cm}^{-1}$. These flat optical modes should contribute little towards heat transport.

The notable feature in the dispersion curves for each of the filled clathrates is the compression of the band width of the highly dispersive heat carrying acoustic phonons from about 100 cm^{-1} in Si_{136} (Fig. 6.1), to about 50 cm^{-1} or lower in $\text{Na}_{16}\text{Rb}_8\text{Si}_{136}$, $\text{K}_{16}\text{Rb}_8\text{Si}_{136}$, $\text{Rb}_8\text{Ga}_8\text{Si}_{128}$, $\text{Cs}_8\text{Ga}_8\text{Si}_{128}$ and $\text{Rb}_8\text{Si}_{136}$. This is due to the very flat localized modes of the Rb or Cs atoms, which lie approximately at the middle of the host acoustic mode region. Due to an avoided crossing effect, there is a strong interaction between localized rattler modes and the framework acoustic branches, resulting in a “bending” of these acoustic branches below the guest rattler modes. This should increase the probability of resonant scattering of the host acoustic phonons, and thus should suppress the lattice thermal conductivity.

In this context, it should be noted that, unlike $\text{Rb}_8\text{Si}_{136}$, the Ga substituted $\text{Rb}_8\text{Ga}_8\text{Si}_{128}$ and $\text{Cs}_8\text{Ga}_8\text{Si}_{128}$ clathrates are semiconducting, which should reduce their electronic contribution to the total thermal conductivity. That could mean even lower thermal conductivity for the framework substituted materials compared to that of $\text{Rb}_8\text{Si}_{136}$, $\text{Na}_{16}\text{Rb}_8\text{Si}_{136}$ and $\text{K}_{16}\text{Rb}_8\text{Si}_{136}$.

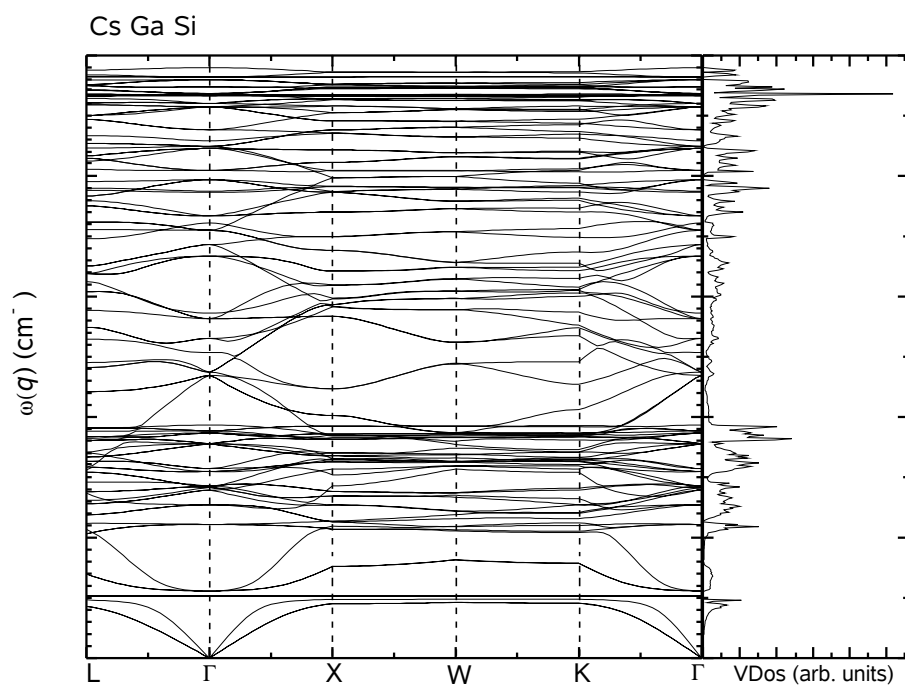
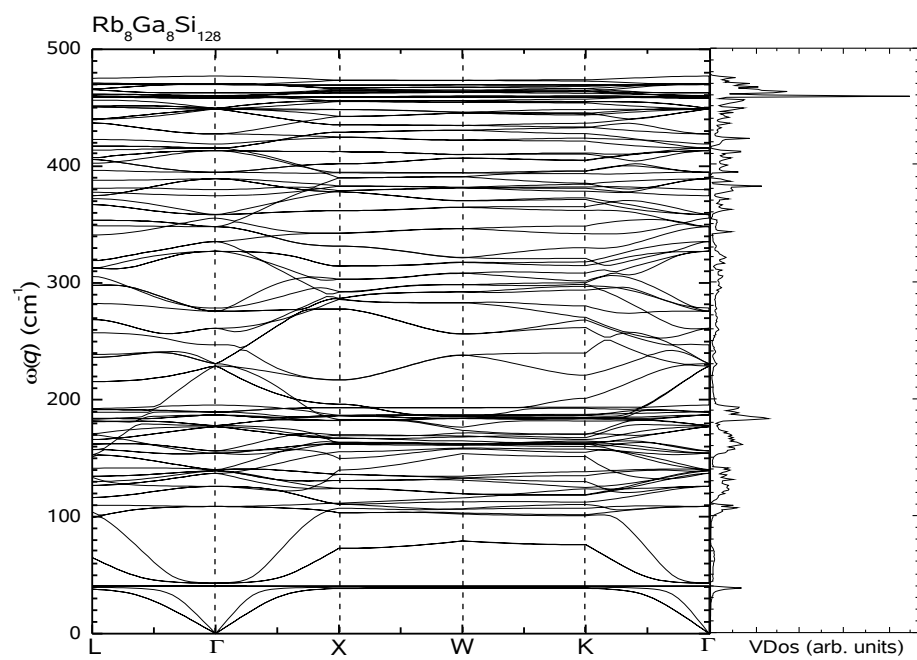


Figure 6.3: Phonon dispersion relations and vibrational density of states (VDos) of $\text{Rb}_8\text{Ga}_8\text{Si}_{128}$ and $\text{Cs}_8\text{Ga}_8\text{Si}_{128}$.

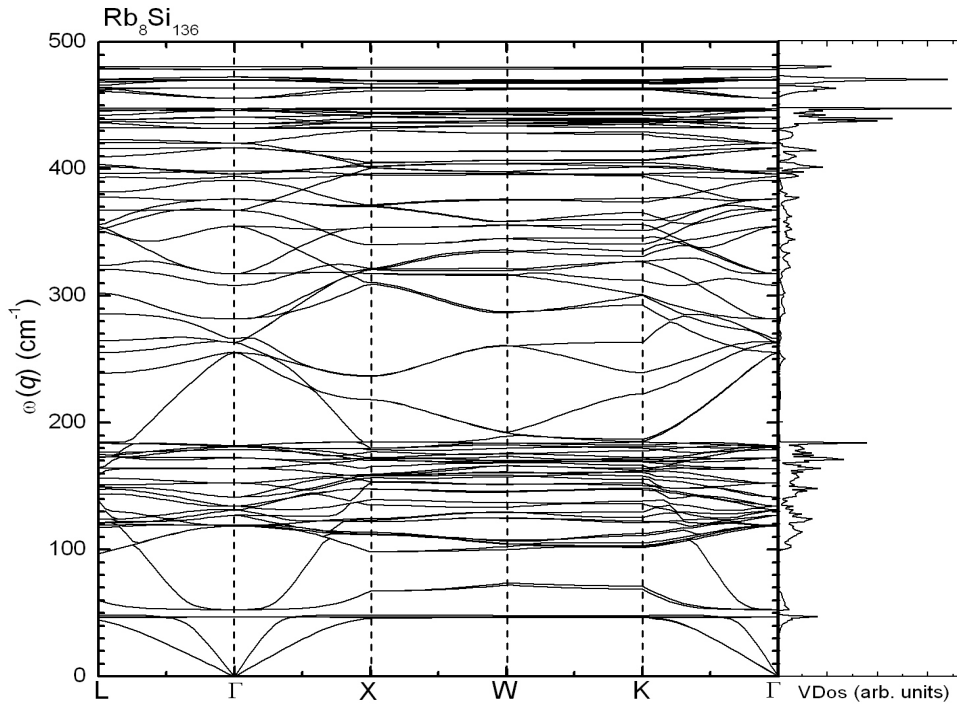


Figure 6.4: Phonon dispersion relations and vibrational density of states (VDos) of $\text{Rb}_8\text{Si}_{136}$.

There is an increased VDos in $\text{Na}_{16}\text{Rb}_8\text{Si}_{136}$ at the bottom of the optic band, in the range of $120\text{-}200\text{ cm}^{-1}$. A similar increase is found in $\text{K}_{16}\text{Rb}_8\text{Si}_{136}$ in the range $140\text{-}200\text{ cm}^{-1}$. This is due to the additional modes coming from the Na or K vibrations, which are absent in $\text{Rb}_8\text{Ga}_8\text{Si}_{128}$, $\text{Cs}_8\text{Ga}_8\text{Si}_{128}$ and $\text{Rb}_8\text{Si}_{136}$.

We also find a “red shift” of the highest optical modes in $\text{Na}_{16}\text{Rb}_8\text{Si}_{136}$ and $\text{K}_{16}\text{Rb}_8\text{Si}_{136}$ compared to the pristine Si_{136} and the $\text{Rb}_8\text{Ga}_8\text{Si}_{128}$ and $\text{Cs}_8\text{Ga}_8\text{Si}_{128}$ clathrates. The frequency downshift for $\text{Na}_{16}\text{Rb}_8\text{Si}_{136}$ is more than 30 cm^{-1} with respect to Si_{136} . Those high frequency optic modes are due to the bond-stretching modes.

In the rigid band picture, the donated electrons from Na (or K) and Rb in the metallic material $\text{Na}_{16}\text{Rb}_8\text{Si}_{136}$ (or $\text{K}_{16}\text{Rb}_8\text{Si}_{136}$) primarily occupy the Si framework antibonding states. These electrons reduce the Si – Si bond order, and therefore, diminish

the stretching force of the Si – Si bonds [60]. This reduces the frequency of the bond stretching modes in $\text{Na}_{16}\text{Rb}_8\text{Si}_{136}$ and $\text{K}_{16}\text{Rb}_8\text{Si}_{136}$, resulting in a downward shift of the highest modes. By contrast, $\text{Rb}_8\text{Ga}_8\text{Si}_{128}$ and $\text{Cs}_8\text{Ga}_8\text{Si}_{128}$ are semiconductors. In those materials, the donated electrons from Rb or Cs primarily occupy the bonding states of the substituted Ga atoms, in order to facilitate their covalent bonding with Si neighbors.

Our LDA calculated average Si – Ga distances are about 2.37 and 2.38 Å in $\text{Cs}_8\text{Ga}_8\text{Si}_{128}$ and $\text{Rb}_8\text{Ga}_8\text{Si}_{128}$, respectively. These are similar to the average Si – Si distances in the two clathrates (see Table 6.1). The slightly larger bond length between Si and Ga may be due to the larger atomic radius of the Ga atom. This implies that the Si – Ga bonds are not appreciably different than the Si – Si bonds. Therefore, the high frequency stretch modes should not be greatly affected in $\text{Rb}_8\text{Ga}_8\text{Si}_{128}$ and $\text{Cs}_8\text{Ga}_8\text{Si}_{128}$, which is consistent with our results.

It has also been shown in Raman scattering experiments [76], that low guest content does not produce a frequency downshift in the Si_{136} clathrates. Consistent with experimental observation, we see no such frequency downshift of the optical modes in $\text{Rb}_8\text{Si}_{136}$. There are less delocalized guest atom states in the partially filled $\text{Rb}_8\text{Si}_{136}$ compared to the completely filled $\text{Na}_{16}\text{Rb}_8\text{Si}_{136}$ and $\text{K}_{16}\text{Rb}_8\text{Si}_{136}$. Hence the high frequency stretch modes in that material are not as much affected as those in $\text{Na}_{16}\text{Rb}_8\text{Si}_{136}$ and $\text{K}_{16}\text{Rb}_8\text{Si}_{136}$, probably resulting in no observable frequency downshift for $\text{Rb}_8\text{Si}_{136}$.

Table 6.1: LDA calculated nearest neighbor distances in $\text{Na}_{16}\text{Rb}_8\text{Si}_{136}$, $\text{K}_{16}\text{Rb}_8\text{Si}_{136}$, $\text{Rb}_8\text{Ga}_8\text{Si}_{128}$, $\text{Cs}_8\text{Ga}_8\text{Si}_{128}$ and $\text{Rb}_8\text{Si}_{136}$.

Clathrate	Si – Si (Å)	Si – Rb (Å)	Si – Ga (Å)	Si – Na (Å)	Si – Cs (Å)
$\text{Na}_{16}\text{Rb}_8\text{Si}_{136}$	2.35 - 2.38	3.90 - 3.98	-	3.17 - 3.35	-
$\text{K}_{16}\text{Rb}_8\text{Si}_{136}$	2.34 - 2.39	3.89 - 3.98	-	-	-
$\text{Rb}_8\text{Ga}_8\text{Si}_{128}$	2.34 - 2.40	3.92 - 3.98	2.38	-	-
$\text{Cs}_8\text{Ga}_8\text{Si}_{128}$	2.33 - 2.39	-	2.37	-	3.89 - 3.96
$\text{Rb}_8\text{Si}_{136}$	2.32 - 2.37	3.88 - 3.95	-	-	-

It is also worth comparing the predicted rattler frequencies for $\text{Rb}_8\text{Ga}_8\text{Si}_{128}$ and $\text{Cs}_8\text{Ga}_8\text{Si}_{128}$. The Rb guests are predicted to have frequencies in the range 40-42 cm^{-1} , while the Cs frequencies lie within the 50-52 cm^{-1} range. The Rb modes are thus considerably lower than the Cs modes, although the Cs atom is about 1.5 times heavier than the Rb atom. This indicates that Cs must be more strongly bound than Rb in the hexakaidecahedra cages. This may be due to the larger size of the Cs in comparison with Rb. We have found a similar trend when we compared the predicted guest atom frequencies in $\text{Na}_{16}\text{Rb}_8\text{Si}_{136}$ with those in $\text{Na}_{16}\text{Cs}_8\text{Si}_{136}$ [28]. Both of these materials show localized Na modes at about 120 cm^{-1} . The striking differences between the two compounds are the localized modes due to Rb and Cs. In an earlier work, it was predicted that the Cs atoms in $\text{Na}_{16}\text{Cs}_8\text{Si}_{136}$ vibrate at frequencies in the range 65-67 cm^{-1} [28]. The present study shows that the Rb modes in $\text{Na}_{16}\text{Rb}_8\text{Si}_{136}$ lie at about 49 cm^{-1} . It is conceivable that the Cs atom, because of its larger size, interacts more with its neighbors, causing it to be more strongly bound than Rb. The stronger guest atom-host atom interaction for Cs in $\text{Na}_{16}\text{Cs}_8\text{Si}_{136}$ is also evident from the lower experimental values of its

atomic displacement parameter (ADP), in comparison to that of Rb in $\text{Na}_{16}\text{Rb}_8\text{Si}_{136}$ in the temperature region 150-300 K [30].

Figure 6.5 shows the predicted phonon dispersion curves and VDos of Ge_{136} . For Ge_{136} , the acoustic modes are below 60 cm^{-1} and the optic modes extend from about $60\text{--}290\text{ cm}^{-1}$. As mentioned earlier, the optical modes do not contribute much towards heat transport.

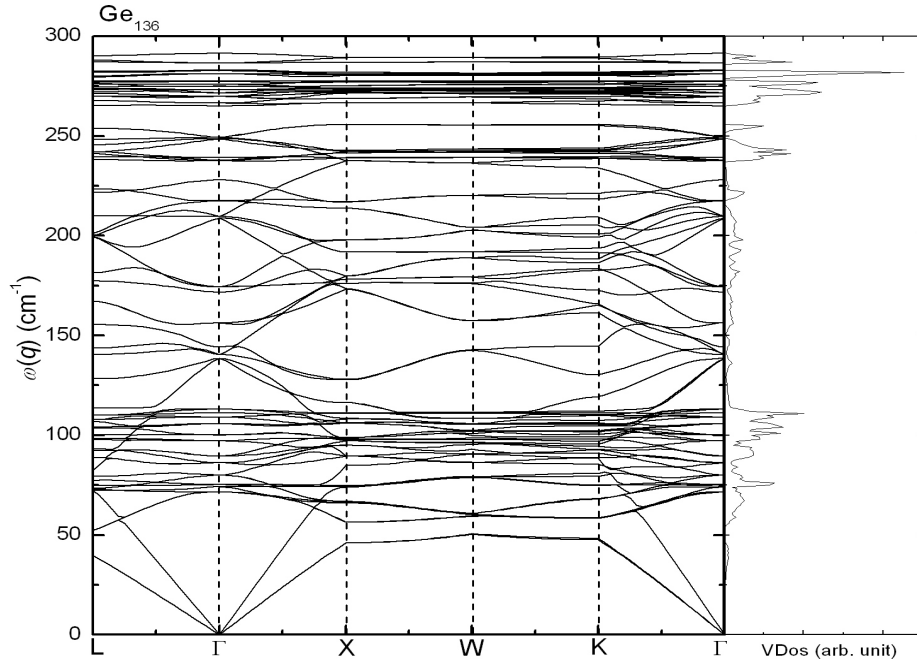


Figure 6.5: Phonon dispersion relations and vibrational density of states (VDos) of Ge_{136} .

In $\text{Na}_{16}\text{Rb}_8\text{Ge}_{136}$ and $\text{Na}_{16}\text{Cs}_8\text{Ge}_{136}$ (Fig. 6.6) the acoustic modes are pushed below 40 cm^{-1} , due to the localized modes from Rb and Cs. In both the filled Ge clathrates, the optic bands are approximately separated into three regions. For example in $\text{Na}_{16}\text{Cs}_8\text{Ge}_{136}$, there is a low frequency, high density of states region from about 40 cm^{-1} to about 80 cm^{-1} , a medium frequency region extending from about 100 cm^{-1} to about 230 cm^{-1} and a narrow, high frequency region from about 230 cm^{-1} to about 250 cm^{-1} .

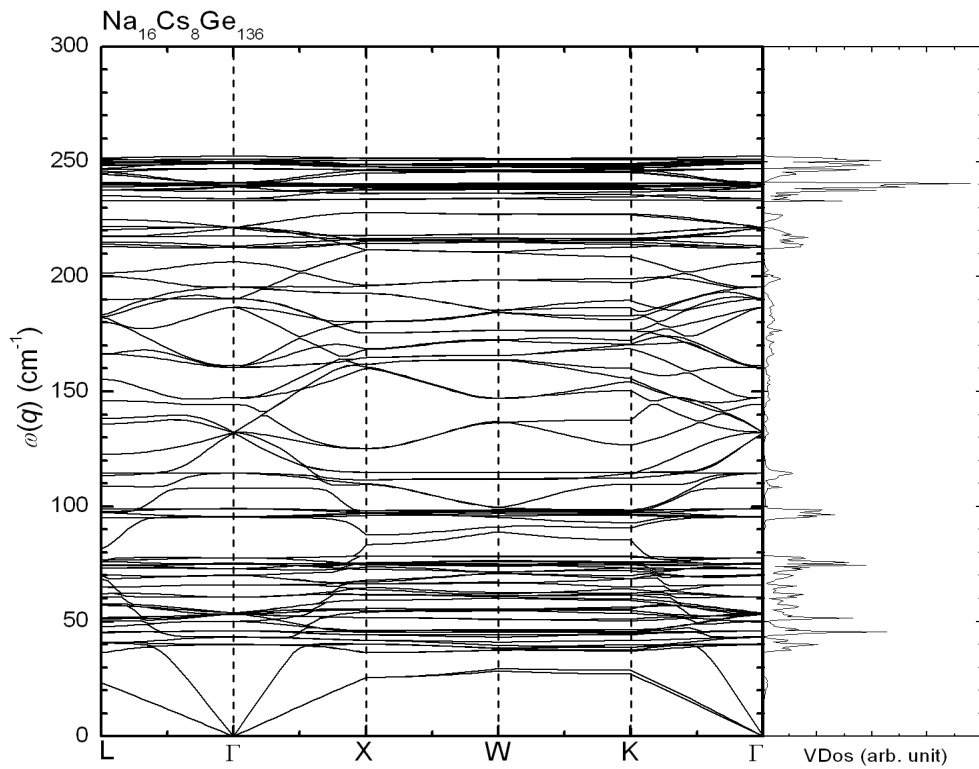
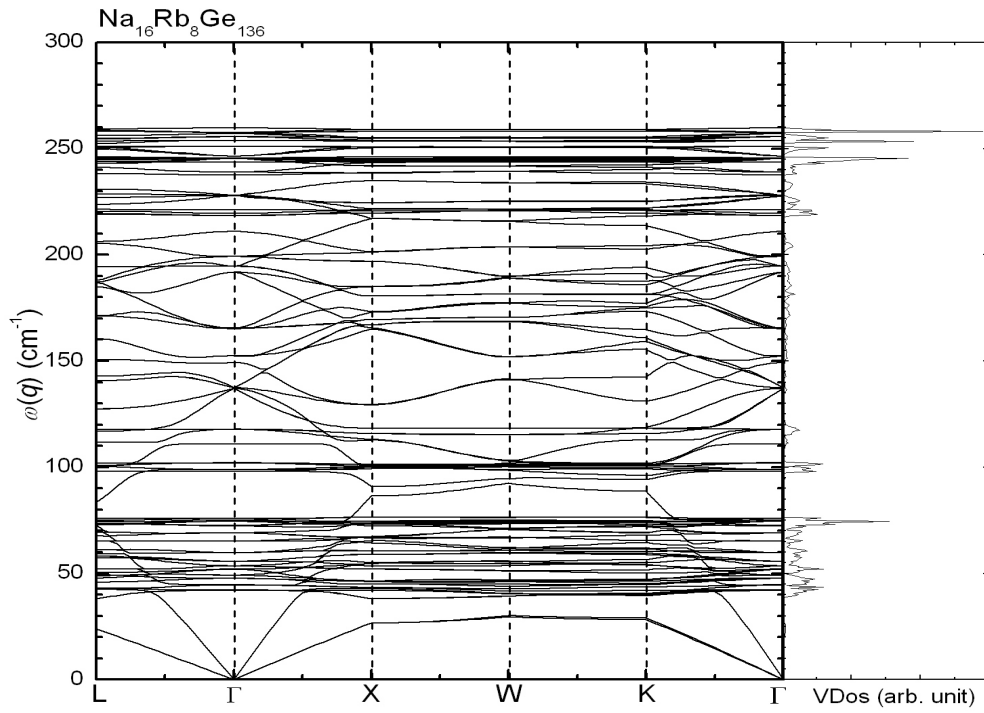


Figure 6.6: Phonon dispersion relations and vibrational density of states (VDos) of $\text{Na}_{16}\text{Rb}_8\text{Ge}_{136}$ and $\text{Na}_{16}\text{Cs}_8\text{Ge}_{136}$.

Like the filled Si clathrates, the $\text{Na}_{16}\text{Rb}_8\text{Ge}_{136}$ and $\text{Na}_{16}\text{Cs}_8\text{Ge}_{136}$ also show a “red shift” in their highest frequencies. The maximum optical frequency for $\text{Na}_{16}\text{Cs}_8\text{Ge}_{136}$ is shifted down by about 40 cm^{-1} compared to that of Ge_{136} .

It must also be noted that the predicted vibrational frequency for Rb in $\text{Na}_{16}\text{Rb}_8\text{Ge}_{136}$ ($\sim 42 \text{ cm}^{-1}$) is very close to that of Cs in $\text{Na}_{16}\text{Cs}_8\text{Ge}_{136}$ ($\sim 40 \text{ cm}^{-1}$). The case of the Si clathrates showed a trend where Rb was predicted to have lower frequency than Cs. We do not find a similar trend in the filled Ge clathrates.

The cages in Ge_{136} are slightly larger than those in Si_{136} . To some extent this may compensate for the larger atomic radius of Cs compared to Rb. Also, since Cs is about 1.5 times heavier than Rb, it is expected that Cs should have much lower vibrational frequency compared to that of Rb. Instead, our results show that their frequencies are almost the same. This means that our assumption of Cs being more strongly bound because of its larger size, holds even in the case of the Ge clathrates. This is supported by experimental data which showed that Rb in $\text{Na}_{16}\text{Rb}_8\text{Ge}_{136}$ had higher ADP than Cs in $\text{Na}_{16}\text{Cs}_8\text{Ge}_{136}$ [30].

Moreover, experimentally predicted values (prediction based on ADP data) of Rb and Cs frequencies in $\text{Na}_{16}\text{Rb}_8\text{Ge}_{136}$ and $\text{Na}_{16}\text{Cs}_8\text{Ge}_{136}$ seem to agree well with our predicted frequencies [30].

The dispersion curves for the Si and Ge clathrates are qualitatively similar. However, due to the heavier mass of Ge, the spectrum for the Ge clathrates are compressed into a smaller energy range than the Si clathrates. A rough estimate of the mass difference between the Si and Ge atoms reveals this effect beautifully. The Si_{136} spectrum extends up to about 490 cm^{-1} while the Ge_{136} spectrum extends up to about 290 cm^{-1} . Therefore, $490/290 \approx 1.69$. Now, $\sqrt{M_{\text{Ge}}}/\sqrt{M_{\text{Si}}} \approx 1.6$, where M_{Ge} and M_{Si} are the

atomic weights of Ge and Si respectively. The ratio of the square root of the masses of Ge and Si is very close to the predicted upward shift in frequency for Si₁₃₆, which is about 1.69 times that of Ge₁₃₆.

6.1 Isotropic Mean Square Displacement Amplitude (U_{iso})

At temperatures where $\hbar\omega < 2k_B T$, an estimate of the mean square displacement amplitude for a guest atom can be obtained in the Einstein model, by using the classical expression $U_{iso} \approx k_B T/K$, where K is the force constant of the oscillator and k_B is the Boltzmann constant. The value of U_{iso} is particularly useful in determining the amount of localized disorder created by the various guest atoms inside the cages. Higher values of U_{iso} may be correlated with a lower vibrational frequency of the guests. From our calculated rattler frequencies, we can estimate the effective force constant using, $\omega = \sqrt{K/M}$, where M is the mass of the guest atom. Our estimated values of K for Rb and Na in Na₁₆Rb₈Si₁₃₆ are 0.76 eV/Å² and 1.26 eV/Å², respectively. The values of K for Rb and Cs in Rb₈Ga₈Si₁₂₈ and Cs₈Ga₈Si₁₂₈ are 0.55 eV/Å² and 1.27 eV/Å², respectively. These low values of K , when compared to a similarly computed K for Si – Si bonds in the clathrates (~ 10 eV/Å²) [27], show the weakly bounded nature of the guest atoms inside the cages.

Using our calculated values of the effective force constants, we show in Table 6.2, our estimated values of U_{iso} for Na and Rb in Na₁₆Rb₈Si₁₃₆ at different temperatures ($T = 150$ to 300 K). Those values are also plotted as shown in Fig. 6.7 (discrete symbols). In the quantized harmonic oscillator model [77],

$$U_{iso} = \langle u^2 \rangle = \frac{h}{8\pi^2 mv} \coth\left(\frac{h\nu}{2k_B T}\right) \quad (6.1)$$

where, ν is the frequency of vibration of the oscillator, m is its reduced mass and h is the Planck constant. The solid curves in Fig. 6.7 show a plot of the above equation for the Na and Rb atoms in $\text{Na}_{16}\text{Rb}_8\text{Si}_{136}$.

Table 6.2: Estimated U_{iso} of Na and Rb atoms in $\text{Na}_{16}\text{Rb}_8\text{Si}_{136}$ at different temperatures.

Temperature (K)	$U_{\text{iso, Na}} (\text{\AA}^2)$	$U_{\text{iso, Rb}} (\text{\AA}^2)$
150	0.0103	0.017
200	0.0137	0.022
250	0.0171	0.028
300	0.0205	0.034

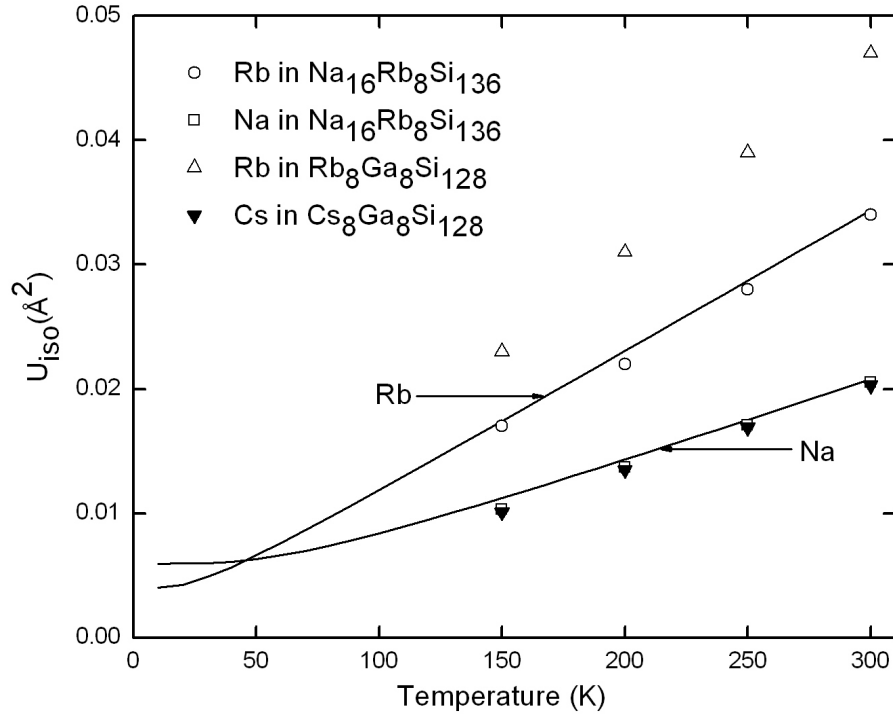


Figure 6.7: Estimated values (discrete symbols) of the isotropic mean square displacement amplitude (U_{iso}) of the various guest atoms at different temperatures. The solid lines are plots of U_{iso} for Rb and Na in $\text{Na}_{16}\text{Rb}_8\text{Si}_{136}$, based on the quantized harmonic oscillator model.

Considering that the clathrate cages are quite rigid, we have assumed in equation 6.1, that the reduced mass of the oscillator is equal to the guest atom mass. As seen in Fig. 6.7, one expects a close resemblance between the quantized and the classical model in the limit $\hbar\omega < 2k_B T$.

Our estimated values of U_{iso} (Table 6.2) obtained from the classical expression ($U_{\text{iso}} \approx k_B T/K$) and our predicted frequencies (ω), are in fairly good agreement with experiment [30]. Of course, our rattler frequencies are calculated at $T = 0$ K. This agreement between experiment and theory indicates that the harmonic oscillator model is a good approximation for predicting the U_{iso} of the rattlers at finite temperatures. The estimated U_{iso} for Na and Rb in $\text{Na}_{16}\text{Rb}_8\text{Si}_{136}$ are expected to be within 10% of the experimental values.

Figure 6.7 also shows our estimated values of U_{iso} (obtained from the classical expression) for Rb and Cs in $\text{Rb}_8\text{Ga}_8\text{Si}_{128}$ and $\text{Cs}_8\text{Ga}_8\text{Si}_{128}$, in the temperature range 150-300 K. It is interesting that Rb has much higher values of U_{iso} than Cs in the temperature range considered. This is due to the larger values of K for Cs than for Rb. Cs is heavier and has a higher vibrational frequency, resulting in a smaller U_{iso} . This result is consistent with experimentally obtained values of U_{iso} for Cs and Rb in $\text{Na}_{16}\text{Cs}_8\text{Si}_{136}$ and $\text{Na}_{16}\text{Rb}_8\text{Si}_{136}$, where it has been shown that Cs has much lower values compared to Rb [30].

Figures 6.8 and 6.9 show the estimated U_{iso} of Na and Rb in $\text{Na}_{16}\text{Rb}_8\text{Ge}_{136}$ and Na and Cs in $\text{Na}_{16}\text{Cs}_8\text{Ge}_{136}$, respectively. The solid lines are a plot of the U_{iso} based on the quantized harmonic oscillator model (equation 6.1). The agreement between the quantized and classical model is very good.

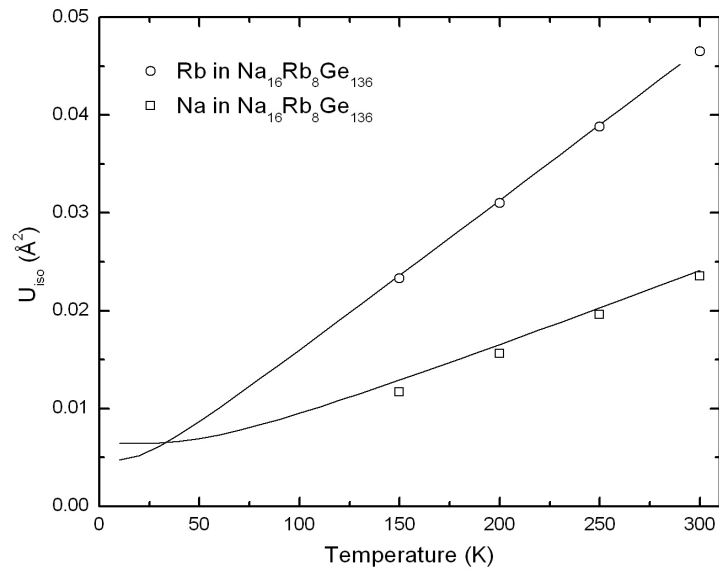


Figure 6.8: Estimated values (discrete symbols) of the isotropic mean square displacement amplitude (U_{iso}) of Na and Rb in $\text{Na}_{16}\text{Rb}_8\text{Ge}_{136}$ at different temperatures. The solid lines are plots of U_{iso} based on the quantized harmonic oscillator model.

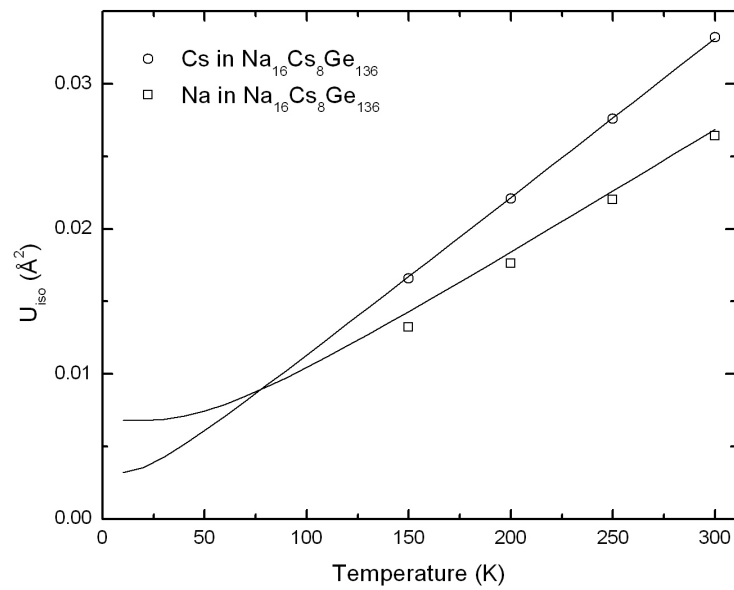


Figure 6.9: Estimated values (discrete symbols) of the isotropic mean square displacement amplitude (U_{iso}) of Na and Cs in $\text{Na}_{16}\text{Cs}_8\text{Ge}_{136}$ at different temperatures. The solid lines are plots of U_{iso} based on the quantized harmonic oscillator model.

The estimated values of U_{iso} for the guest atoms in $\text{Na}_{16}\text{Cs}_8\text{Ge}_{136}$ shown in Table 6.3, are not in good agreement with reported experimental data [30]. The estimated U_{iso} of Na and Rb in $\text{Na}_{16}\text{Rb}_8\text{Ge}_{136}$ (Table 6.4), though not as good an agreement as in the Si clathrates, are close to the reported experimental values [30]. It is not clear why the agreement between experiment and our predicted results are not as good in the Ge clathrates as they are for the Si clathrates. Paradoxically, the estimated rattler frequencies of the Na, Rb and Cs atoms in the Ge clathrates reported from the ADP data are in much better agreement with our predicted frequencies [30]. Given that our calculations are based on the harmonic approximation, this probably means that there is a greater anharmonic contribution to the ADP of these atoms in the Ge clathrates which results in the mismatch between the predicted and experimental data.

Table 6.3: Estimated U_{iso} of Na and Cs atoms in $\text{Na}_{16}\text{Cs}_8\text{Ge}_{136}$ at different temperatures.

Temperature (K)	$U_{\text{iso}, \text{Na}} (\text{\AA}^2)$	$U_{\text{iso}, \text{Cs}} (\text{\AA}^2)$
150	0.0132	0.0166
200	0.0176	0.0221
250	0.022	0.0276
300	0.0264	0.0332

Table 6.4: Estimated U_{iso} of Na and Rb atoms in $\text{Na}_{16}\text{Rb}_8\text{Ge}_{136}$ at different temperatures.

Temperature (K)	$U_{\text{iso}, \text{Na}} (\text{\AA}^2)$	$U_{\text{iso}, \text{Rb}} (\text{\AA}^2)$
150	0.0117	0.0233
200	0.0156	0.031
250	0.0196	0.0388
300	0.0235	0.0465

With our estimated values of U_{iso} at 300 K, we have predicted the Einstein temperatures (θ_E) of the various guest atoms using,

$$U_{\text{iso}} = k_B T / K = h^2 T / (4\pi^2 m k_B \theta_E^2) \quad (6.2)$$

The predicted values for guests in various Si and Ge clathrates are shown in Table 6.5. The calculated values of U_{iso} at 300 K were used to predict θ_E . The high value of θ_E for Na in the different Si and Ge clathrates is consistent with its lower U_{iso} and its smaller mass.

In a recent paper [78], it has been suggested that the glass-like thermal conductivity in clathrates is a consequence of three different phonon scattering mechanisms. It was shown, based on empirical evidence, that the phonons scattered from free charge carriers and bound/localized charge carriers were the dominant scattering mechanisms at temperatures below 50 K, and that the resonant scattering of host phonons by guest atoms occurred at temperatures above 50-70 K [78]. It is interesting that all of our estimated values of θ_E of the various guests are above 50 K. This may also imply that the resonant scattering of host phonons would be dominant at temperatures above 50 K.

Table 6.5: Predicted Einstein temperatures (θ_E), of the various guest atoms in $\text{Na}_{16}\text{Rb}_8\text{Si}_{136}$, $\text{Rb}_8\text{Ga}_8\text{Si}_{128}$, $\text{Cs}_8\text{Ga}_8\text{Si}_{128}$, $\text{Na}_{16}\text{Rb}_8\text{Ge}_{136}$ and $\text{Na}_{16}\text{Cs}_8\text{Ge}_{136}$.

Clathrate	$\theta_{E,Na}$ (K)	$\theta_{E,Rb}$ (K)	$\theta_{E,Cs}$ (K)
$\text{Na}_{16}\text{Rb}_8\text{Si}_{136}$	175	70.5	-
$\text{Rb}_8\text{Ga}_8\text{Si}_{128}$	-	60	-
$\text{Cs}_8\text{Ga}_8\text{Si}_{128}$	-	-	73
$\text{Na}_{16}\text{Rb}_8\text{Ge}_{136}$	164	60.5	-
$\text{Na}_{16}\text{Cs}_8\text{Ge}_{136}$	155.5	-	57.6

CHAPTER VII
THERMODYNAMIC PROPERTIES OF
Si₁₃₆ AND Ge₁₃₆

First principles theoretical methods have been used here to predict the temperature dependence of the vibrational contributions to the free energy, the entropy and the specific heat capacity at constant volume (C_V) of the empty Si₁₃₆ and Ge₁₃₆ clathrates. All quantities are predicted using the harmonic approximation. Because most experiments are conducted at constant pressure, it would be more relevant to calculate the Gibbs free energy. However, the Helmholtz free energy has been calculated in this study. Like most semiconductors, these type II clathrates also have a low coefficient of thermal expansion. Si₁₃₆, for example, is reported to have a thermal expansion coefficient which is less than $4 \times 10^{-6} \text{ K}^{-1}$ up to a temperature of about 800 K [79]. Therefore, the difference between the specific heat at constant pressure and at constant volume ($C_P - C_V$) should not be too large and it may be appropriate to compare calculated C_V with experimental C_P data. The difference between the two heat capacities is given by the equation, $C_P - C_V = \alpha^2 TVK$, where α is the temperature dependent volume coefficient of thermal expansion and K is the bulk modulus.

The Helmholtz free energy is given by,

$$F(T) = E_{static} + F_{vib}(T) \quad (7.1)$$

where, E_{static} is the static lattice energy when all atoms are fixed at their lattice positions and $F_{vib}(T)$ is the vibrational free energy. Figure 7.1(a, b) shows the predicted temperature dependence of the vibrational free energies $F_{vib}(T)$, of Si₁₃₆ and Ge₁₃₆ in the range 0-600 K.

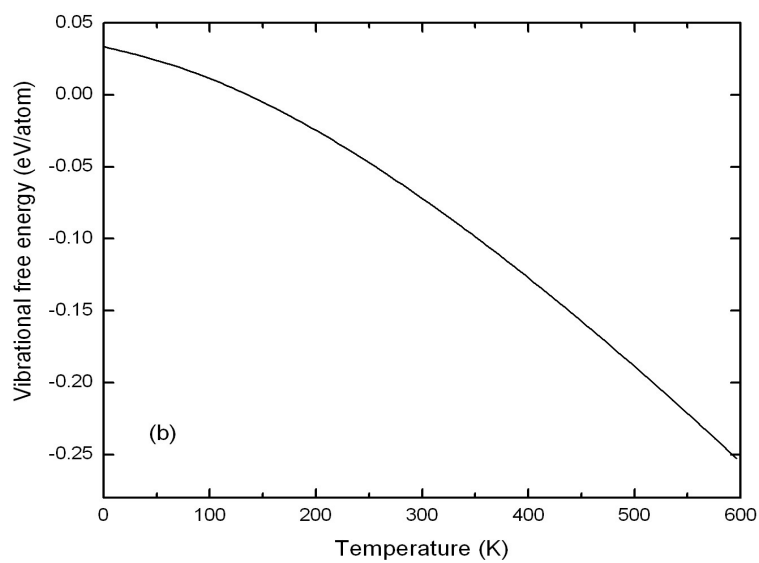
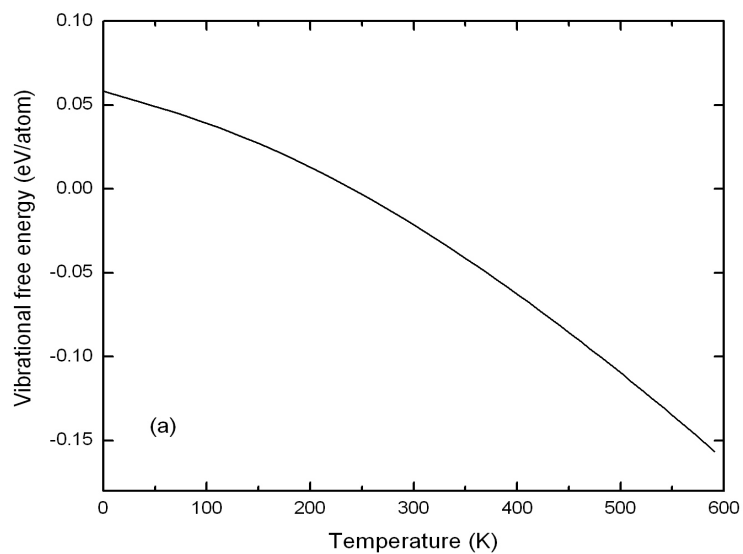


Figure 7.1: Predicted temperature dependence of vibrational free energy of (a) Si₁₃₆ and (b) Ge₁₃₆ in the range 0-600 K.

Recently, Miranda et al. [80] reported the Gibbs free energy of the Si₁₃₆ clathrate.

Their calculations were based on the reversible scaling Monte Carlo (RS-MC) method

[80]. Although a direct comparison between Helmholtz and Gibbs free energy is not possible, our calculated zero-point energy $F_{vib}(T=0)$, of about 0.062 eV/atom agree with that reported by Miranda et al. (see Fig. 1 in Ref. 80).

Figures 7.2 and 7.3 shows the calculated vibrational entropies of Si_{136} and Ge_{136} as a function of temperature. There is a large entropy difference between the Si_{136} and Ge_{136} clathrates. The temperature variation of the entropy of Si_{136} is in good agreement with the LDA results reported recently by Tang et al. [79].

One notable feature is the close proximity of the entropy values of each clathrate with their respective diamond phases. The predicted entropies of both Si_{136} and Ge_{136} are slightly higher than their corresponding diamond phases. This is expected because the open framework structure of the clathrates should lead to a larger vibrational entropy. The experimental values of the entropy of diamond structured Ge (*d*-Ge) and *d*-Si [81] and the predicted entropies of Si_{136} and Ge_{136} at 300 K are shown in Table 7.1.

Miranda et al. [80] also reported calculations of the vibrational entropy of Si_{136} between the temperatures 0 to 2000 K. Their results are in good agreement with our calculations. For example, their calculated value of the vibrational entropy of Si_{136} at 1522 K (predicted melting point of Si_{136}) was 62.9 J/mole-K, compared to our predicted value of 61.0 J/mole-K at 1521 K.

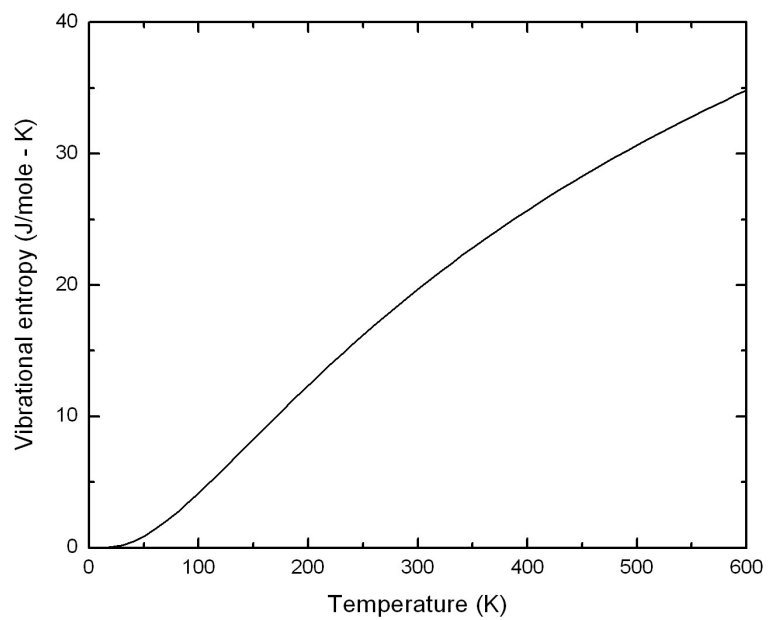


Figure 7.2: Predicted vibrational entropy of Si_{136} in the temperature range 0-600 K.

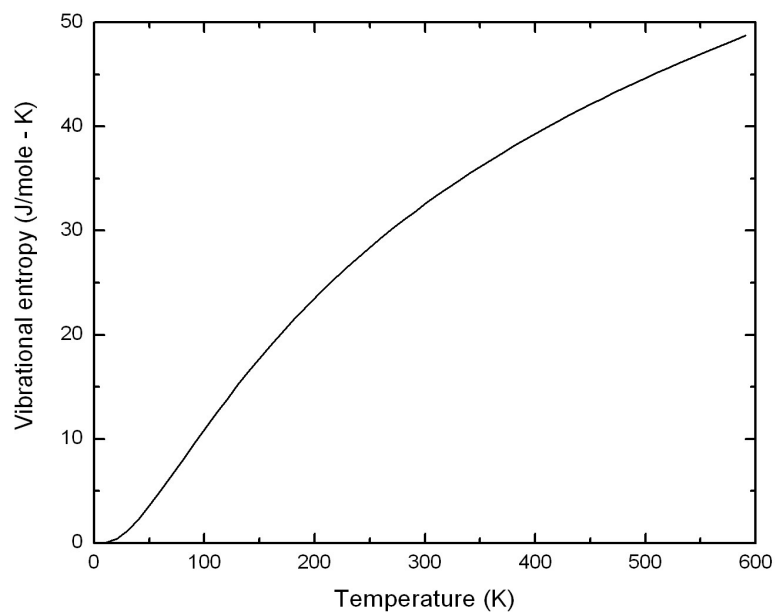


Figure 7.3: Predicted vibrational entropy of Ge_{136} in the temperature range 0-600 K.

Table 7.1: Predicted entropies of Si_{136} and Ge_{136} at 300 K, and the corresponding experimental values of $d\text{-Si}$ and $d\text{-Ge}$ at the same temperature [81].

Si_{136} Theory	19.75 J/mole-K
$d\text{-Si}$ Expt.	18.82 J/mole-K
Ge_{136} Theory	32.63 J/mole-K
$d\text{-Ge}$ Expt.	31.23 J/mole-K

As mentioned before, the difference $C_P - C_V$ is expected to be low for the clathrates, so that a comparison of the predicted C_V with experimental C_P should be qualitatively meaningful. Figure 7.4 shows the temperature dependence of predicted C_V of Si_{136} (solid line) in the range 0-300 K.

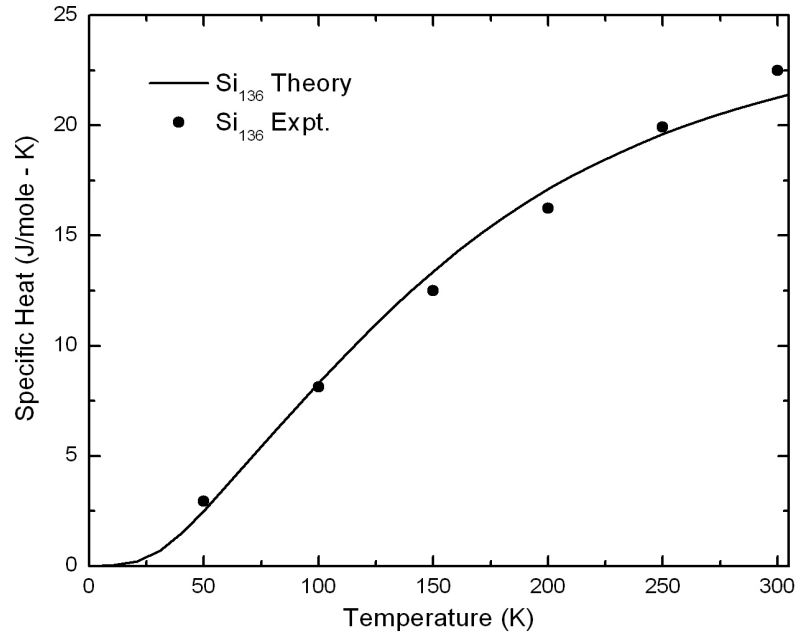


Figure 7.4: Calculated specific heat (C_V) (solid line) and measured isobaric specific heat (C_P) (discrete symbols) of Si_{136} in the range 0-300 K [58].

Nolas et al. has measured the C_P of Si_{136} up to 300 K [51]. Those initial data were not in good agreement with our calculated values. However, that group recently remeasured the C_P of Si_{136} and their updated results [58] are in better agreement as shown in Fig. 7.4.

The calculated C_V of Si_{136} is found to be slightly larger than the experimental C_P of $d\text{-Si}$ up to about 270 K. Since C_P is greater than C_V , it is predicted that the clathrate phase of Si has higher specific heat (by about 0.33 J/mole-K) than that of $d\text{-Si}$ at about 200 K [82]. At higher temperatures the predicted values are supposed to deviate from actual values because of the increase in anharmonicity of the different vibrational modes.

The temperature dependence of the calculated C_V of Ge_{136} is shown in Fig. 7.5. Here again, Ge_{136} is predicted to have slightly larger values of specific heat compared to $d\text{-Ge}$ at least up to 200 K (21.22 J/mole-K for Ge_{136} at 200K compared to 20.88 J/mole-K for $d\text{-Ge}$ at th same temperature) [83]. Currently, there are no experimental data available on the specific heat capacity of Ge_{136} .

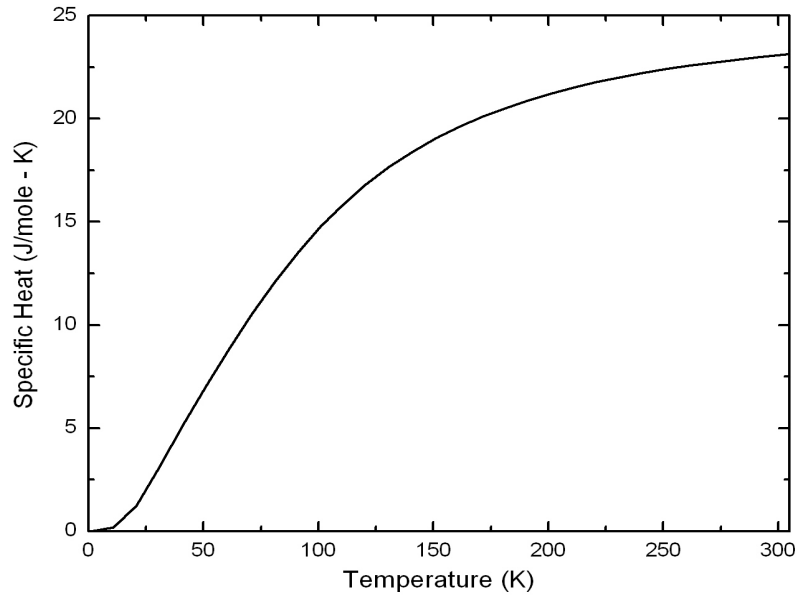


Figure 7.4: Calculated specific heat (C_V) of Ge_{136} in the range 0-300 K.

CHAPTER VIII

CONCLUSIONS

Group IV semiconductor clathrates have emerged as an interesting class of materials, with potential applications in the field of thermoelectrics. They are very interesting from a fundamental physics view point, which was the basis for this research. We have used the LDA to study the equations of state, electronic, vibrational and the thermodynamic properties of several type II clathrate materials.

The electronic band structures of the filled clathrates agree qualitatively with the rigid band model. Our results show that the bands for non-framework substituted guest containing materials are nearly the same as those of the guest free materials and that there is a charge transfer from the guests into the host conduction states. This raises the Fermi level into the conduction band of the $\text{Na}_{16}\text{Rb}_8\text{Si}_{136}$, $\text{K}_{16}\text{Rb}_8\text{Si}_{136}$, $\text{Na}_{16}\text{Rb}_8\text{Ge}_{136}$, and the $\text{Na}_{16}\text{Cs}_8\text{Ge}_{136}$ clathrates, as discussed in Chapter V.

The electronic density of states (DOS) near the Fermi level of the $\text{Na}_{16}\text{Rb}_8\text{Si}_{136}$, $\text{K}_{16}\text{Rb}_8\text{Si}_{136}$, $\text{Na}_{16}\text{Rb}_8\text{Ge}_{136}$, and the $\text{Na}_{16}\text{Cs}_8\text{Ge}_{136}$ clathrates also show a charge transfer from the different guest atoms to the Si or Ge framework. The DOS near the Fermi level is higher for these filled clathrates compared to Si_{136} or Ge_{136} . However, for the framework substituted $\text{Rb}_8\text{Ga}_8\text{Si}_{128}$ and $\text{Cs}_8\text{Ga}_8\text{Si}_{128}$ clathrates there is no such increase in DOS. This is due to the unpaired p -orbitals in the Ga atoms.

We predict that $\text{Rb}_8\text{Ga}_8\text{Si}_{128}$ and $\text{Cs}_8\text{Ga}_8\text{Si}_{128}$ are semiconducting with indirect LDA band gaps approximately in the range 0.73-0.77 eV. Thus framework substitution may help to reduce the electronic contribution to the total thermal conductivity. A

comparison of the DOS of $\text{Rb}_8\text{Ga}_8\text{Si}_{128}$ with those of $\text{Rb}_8\text{Si}_{136}$ also emphasizes the role of Ga-substitution.

The calculated projected densities of states of the $\text{Na}_{16}\text{Rb}_8\text{Si}_{136}$, $\text{K}_{16}\text{Rb}_8\text{Si}_{136}$, $\text{Na}_{16}\text{Rb}_8\text{Ge}_{136}$, and the $\text{Na}_{16}\text{Cs}_8\text{Ge}_{136}$ clathrates qualitatively explain the observed temperature dependent Knight shift. The results show the s-like character of the states near the Fermi level of these materials, irrespective of the presence of peak-like structures in the DOS. $\text{Na}_{16}\text{Rb}_8\text{Si}_{136}$ and $\text{K}_{16}\text{Rb}_8\text{Si}_{136}$ do show peaks near the Fermi level. However, the peak separation (200-400 meV) is much larger than the $k_B T$ at which the temperature dependent Knight shifts have been observed. The predominance of the donor derived s-like states in the lower portion of the conduction band is the more likely reason for the observed temperature dependent shifts.

All the filled clathrates are predicted to have low frequency guest vibrational modes that are near the middle of the host acoustic band, which effectively compresses the acoustic mode band width. This implies an efficient scattering of the host acoustic phonons, which is essential for reducing the lattice thermal conductivity.

Even though Cs is heavier than Rb, in the case of the Si clathrates we predict that Rb has a lower vibrational frequency than Cs. This could mean a more efficient phonon scattering mechanism for Rb than Cs.

Compared to Si_{136} and Ge_{136} , there is a frequency down-shift in the highest optical phonon modes for the $\text{Na}_{16}\text{Rb}_8\text{Si}_{136}$, $\text{K}_{16}\text{Rb}_8\text{Si}_{136}$, $\text{Na}_{16}\text{Rb}_8\text{Ge}_{136}$, and the $\text{Na}_{16}\text{Cs}_8\text{Ge}_{136}$ clathrates. This is due to the antibonding character of the states occupied by the electrons from the donor guest atoms. More interestingly, the phonon dispersion curves of the $\text{Rb}_8\text{Ga}_8\text{Si}_{128}$ and $\text{Cs}_8\text{Ga}_8\text{Si}_{128}$ clathrates do not show such a large frequency downshift.

This is because the electrons from the guest atoms now occupy the bonding states of the unpaired p -orbitals of the Ga atoms.

Our estimated temperature-dependent values of the mean square displacement amplitude (U_{iso}) for Rb and Na in $\text{Na}_{16}\text{Rb}_8\text{Si}_{136}$ agree well with experiment, meaning that the anharmonic contributions up to 300 K are small. As expected from our calculated frequencies, we predict higher values of U_{iso} for Rb in $\text{Rb}_8\text{Ga}_8\text{Si}_{128}$ than Cs in $\text{Cs}_8\text{Ga}_8\text{Si}_{128}$. The agreement between the estimated U_{iso} and the experimental values is not as good in the Ge clathrates. However, these values are consistent with the trend where Rb is shown to have higher values of U_{iso} and hence higher localized disorder than the heavier Cs atoms.

The vibrational contributions to the thermodynamic properties of the Si_{136} and Ge_{136} clathrates bear close resemblance to those of their respective diamond phases. A comparison of the predicted temperature dependence of the free energy shows that Si_{136} is more stable than the Ge_{136} phase. The vibrational entropies of Si_{136} and Ge_{136} are slightly higher than those of their corresponding diamond phases. Temperature dependent heat capacities of Si_{136} and Ge_{136} are also predicted to be higher than those in the respective diamond phases.

Finally, the present work can be summarized as follows:

- 1) Non-framework substituted filled clathrates:
 - a) there is a charge transfer from guest atom to host conduction band (metallic character)
 - b) s -orbital character of the states near E_f (derived from guest electrons) provides a qualitative explanation of the observed temperature dependence of the Knight shifts.

- 2) Framework substituted filled clathrates:
 - a) these are semiconducting due to the unpaired valence electrons in Ga; semiconducting behavior is useful in reducing the electronic contribution to the total thermal conductivity
 - b) LDA band gap reduced in comparison to the empty Si_{136} . This is likely due to the Ga p -states near the top of the valence band and guest atom s -states near the bottom of the conduction band.
- 3) Harmonic approximation may be used to theoretically estimate the atomic displacement parameter of the various guest atoms (U_{iso}).
- 4) Rb is predicted to have lower vibrational frequency and higher U_{iso} than Cs; Rb may be a more efficient rattler compared to Cs.
- 5) The Si and Ge clathrate phases have higher entropy and higher heat capacity than their corresponding diamond phases.

BIBLIOGRAPHY

- [1] G. S. Nolas, J. Sharp, and H. J. Goldsmid, *Thermoelectrics – Basic Principles and New Materials Development*, (Springer, 2001).
- [2] *Semiconductors and Semimetals*, edited by T. M. Tritt (Academic Press, San Diego, 2001), Vol. 69.
- [3] A. F. Ioffe, *Semiconductor Thermoelements and Thermoelectric Cooling*, Infosearch, London, p. 39 (1957).
- [4] A. L. Jain, *Phys. Rev.* **114**, 1518 (1959).
- [5] S. Tanuma, *J. Phys. Soc. Japan* **14**, 1246 (1959).
- [6] N. B. Brandt and E. A. Svistova, *J. Low Temp. Phys.* **2**, 1 (1970).
- [7] G. E. Smith and R. Wolfe, *J. Appl. Phys.* **33**, 841 (1962).
- [8] H. J. Goldsmid, K. K. Gopinathan, D. N. Matthews, K. N. R. Taylor, and C. A. Baird, *J. Phys. D* **21**, 344 (1988).
- [9] F. G. Aliev, N. B. Brandt, V. V. Moschalkov, V. V. Kozyrkov, R. V. Scolozdra, and A. I. Belogorokhov, *Z. Phys. B* **75**, 167 (1989).
- [10] F. G. Aliev, V. V. Kozyrkov, V. V. Moschalkov, R. V. Scolozdra, and K. Durczewski, *Z. Phys. B* **80**, 353 (1990).
- [11] B. A. Cook, J. L. Harringa, Z. S. Tan, and W. A. Jesser, *Proceedings 15th International Conference on Thermoelectrics*, p. 122 (1996).
- [12] C. Uher, J. Yang, and S. Hu, *MRS Symp. Proc.* **545**, 247 (1999).
- [13] C. Uher, J. Yang, S. Hu, D. T. Morelli, and G. P. Meisner, *Phys. Rev. B* **59**, 8615 (1999).
- [14] D. Shechtman, I. Blech, D. Gratias, and J. W. Cahn, *Phys. Rev. Lett.* **53**, 1951 (1984).
- [15] M. Chernikov, A. Bianchi, and H. Ott, *Phys. Rev. B* **51**, 153 (1995).
- [16] E. Maciá, *Appl. Phys. Lett.* **77**, 3045 (2000).
- [17] G. A. Slack, in *CRC Handbook of Thermoelectrics*, edited by D. M. Rowe (CRC press, Boca Raton, FL, 1995) p. 407.

- [18] G. S. Nolas, G. A. Slack, J. L. Cohn, and S. B. Schujman, Proceedings 17th International Conference on Thermoelectrics, p. 294 (1998).
- [19] J. L. Cohn, G. S. Nolas, V. Fessatidis, T. H. Metcalf, and G. A. Slack, Phys. Rev. Lett. **82**, 779 (1999).
- [20] K. Moriguchi, M. Yonemura, and A. Shintani, Phys. Rev. B **61**, 9859 (2000).
- [21] G. S. Nolas, T. J. R. Weakley, and J. L. Cohn, Chem. Mater. **11**, 2470 (1999).
- [22] G. S. Nolas, J. L. Cohn, and E. Nelson, Proceedings 19th International Conference on Thermoelectrics, p. 493 (2000).
- [23] G. S. Nolas, J. L. Cohn, and G. A. Slack, Phys. Rev. B **58**, 164 (1998).
- [24] L. D. Hicks and M. S. Dresselhaus, Phys. Rev. B **47**, 12727 (1993).
- [25] J. S. Kasper, P. Hagenmuller, M. Pouchard, and C. Cros, Science **150**, 1713 (1965).
- [26] T. M. Tritt, Science **283**, 804 (1999).
- [27] J. Dong, O. F. Sankey, G. K. Ramachandran, and P. F. Mcmillan, J. Appl. Phys. **87**, 7726 (2000).
- [28] C. W. Myles, J. Dong, and O. F. Sankey, Phys. Stat. Sol. (b) **239**, 26 (2003).
- [29] S. Lattner, B. B. Iversen, J. Sepa, V. Srdanov, and G. Stucky, Phys. Rev. B **63**, 125403 (2001).
- [30] G. S. Nolas, D. G. Vanderver, A. P. Wilkinson, and J. L. Cohn, J. Appl. Phys. **91**, 8970 (2002).
- [31] G. A. Slack, *Solid State Physics*, edited by F. Seitz, D. Turnbull, and H. Ehrenreich, Vol. 34, (Academic, New York, 1979).
- [32] G. S. Nolas, J. L. Cohn, G. A. Slack, and S. B. Schujman, Appl. Phys. Lett. **73**, 178 (1998).
- [33] N. F. Mott, J. Solid State Chem. **6**, 348 (1973).
- [34] C. Cros and J. C. Bénéjat, Bull. Soc. Chim. Fr. **5**, 1739 (1972).
- [45] A. A. Demkov, O. F. Sankey, K. E. Schmidt, G. B. Adams, and M. O'Keeffe, Phys. Rev. B **50**, 17001 (1994).
- [36] V. I. Smelyansky and J. S. Tse, Chem. Phys. Lett. **264**, 459 (1997).
- [37] H. Kawaji, H. O. Horie, S. Yamanaka, and M. Ishikawa, Phys. Rev. Lett. **74**, 1427 (1995).
- [38] *Semiconductors and Semimetals*, edited by T. M. Tritt (Academic Press, San Diego,

2001), Vol. 70, 71.

[39] P. Larson, S. D. Mahanti, S. Sportouch, and M. G. Kanatzidis, *Phys. Rev. B* **59**, 15660 (1999).

[40] D. Young, K. Mastronardi, P. Khalifah, C. C. Wang, and R. J. Cava, *Appl. Phys. Lett.* **74**, 3999 (1999).

[41] *Water, A Comprehensive Treatise*, edited by F. Franks (Plenum Press, New York, 1972).

[42] C. Cros, M. Pouchard, and P. Hagenmuller, *C. R. Acad. Sc. Paris* **260**, 4764 (1965).

[43] C. Cros, M. Pouchard, P. Hagenmuller, and J. S. Kasper, *Bull. Soc. Chim. Fr.* **7**, 2737 (1968).

[44] C. Cros, M. Pouchard, and P. Hagenmuller, *J. Solid State Chem.* **2**, 570 (1970).

[45] M. Beekman and G. S. Nolas, *Physica B* **383**, 111 (2006).

[46] G. B. Adams, M. O'Keeffe, A. A. Demkov, O. F. Sankey, and Y. M. Huang, *Phys. Rev. B* **49**, 8048 (1994).

[47] J. Dong, O. F. Sankey, and G. Kern, *Phys. Rev. B* **60**, 950 (1999).

[48] P. Mélinon, P. Kéghélian, X. Blase, J. Le Brusq, and A. Perez, *Phys. Rev. B* **58**, 12590 (1998).

[49] J. Dong and O. F. Sankey *J. Phys.: Condens. Matter* **11**, 6129 (1999).

[50] P. Mélinon, P. Kéghélian, A. Perez, B. Champagnon, Y. Guyot, L. Saviot, E. Reny, C. Cros, M. Pouchard, and A. J. Dianoux, *Phys. Rev. B* **59**, 10099 (1999).

[51] G. S. Nolas, M. Beekman, J. Gryko, G. A. Lamberton Jr., T. M. Tritt, and P. F. McMillan, *Appl. Phys. Lett.* **82**, 910 (2003).

[52] R. F. Marzke, G. S. Nolas, and J. Gryko in *Thermoelectric Materials 2001—Research and Applications*, edited by G. S. Nolas, D. C. Johnson, D. G. Mandrus, *Mater. Res. Soc. Symp. Proc. No. 691* (Materials Research Society, Warrendale, 2002), p. 439.

[53] F. Birch, *J. Geophys. Res.* **57**, 227 (1952).

[54] J. Gryko, P. F. McMillan, R. F. Marzke, A. P. Dodokin, A. A. Demkov, and O. F. Sankey, *Phys. Rev. B* **57**, 4172 (1998).

[55] K. Moriguchi, S. Munetoh, and A. Shintani, *Phys. Rev. B* **62**, 7138 (2000).

- [56] J. Tersoff, Phys. Rev. B **39**, 5566 (1989); J. Tersoff, Phys. Rev. Lett. **56**, 632 (1986); J. Tersoff, Phys. Rev. B **37**, 6991 (1988); J. Tersoff, Phys. Rev. B **38**, 9902 (1988); J. Tersoff, Phys. Rev. Lett. **61**, 2879 (1988); J. Tersoff, Phys. Rev. Lett. **64**, 1757 (1990); J. Tersoff, Phys. Rev. B **49**, 16349 (1994).
- [57] K. Moriguchi, S. Munetoh, A. Shintani, and T. Motooka, Phys. Rev. B **64**, 195409 (2001).
- [58] G. S. Nolas, Department of Physics, University of South Florida, Tampa, FL, Personal communication (2006).
- [59] P. Hohenberg and W. Kohn, Phys. Rev. **136**, B864, (1964); W. Kohn, and L. J. Sham, Phys. Rev. **140**, A1133 (1965).
- [60] G. S. Nolas, C. A. Kendziora, J. Gryko, J. Dong, C. W. Myles, A. Poddar, and O. F. Sankey, J. Appl. Phys. **92**, 7225 (2002).
- [61] G. Kresse and J. Furthümlller, Comput. Mater. Sci. **6**, 15 (1996); G. Kresse and J. Hafner, Phys Rev. B **47**, 558 (1993); G. Kresse and J. Fürthumlller, Phys. Rev. B **54**, 11169 (1996).
- [62] D. Vanderbilt, Phys Rev. B **41**, 7892 (1990); K. Laasonen, R. Car, C. Lee, and D. Vanderbilt, Phys. Rev. B **43**, 6796 (1991); K. Laasonen, A. Pasquarello, R. Car, C. Lee, and D. Vanderbilt, Phys. Rev. B **47**, 10142 (1993).
- [63] G. Kresse and J. Hafner, Phys. Rev. B **48**, 13115 (1993); G. Kresse and J. Hafner, J. Phys.: Condens. Matter **6**, 8245 (1994).
- [64] D. M. Ceperley and B. J. Alder, Phys. Rev. Lett. **45**, 566 (1980).
- [65] H. J. Monkhorst and J. D. Pack, Phys. Rev. B **13**, 5188 (1976).
- [66] A. A. Maradudin, E. W. Montroll, G. H. Weiss, and I. P. Ipatova, *Theory of Lattice Dynamics in the Harmonic Approximation* (Academic, New York, 1971).
- [67] A. San-Miguel, P. Kéghélian, X. Blase, P. Mélinon, A. Perez, J. P. Itié, A. Polian, E. Reny, C. Cros, and M. Pouchard, Phys. Rev. Lett. **83**, 5290 (1999).
- [68] G. K. Ramachandran, P. F. McMillan, S. K. Deb, M. Somayazulu, J. Gryko, J. Dong, and O. F. Sankey, J. Phys.: Condens. Matter **12**, 4013 (2000).
- [69] S. Bobev and S. C. Sevov, J. Am. Chem. Soc. **121**, 3795 (1999).
- [70] S. Bobev and S. C. Sevov, J. Solid State Chem. **152**, 92 (2000).
- [71] G. K. Ramachandran, J. Dong, O. F. Sankey, and P. F. McMillan, Phys. Rev. B **63**, 033102 (2000).

- [72] C. P. Slichter, *Principles of Magnetic Resonance* (Springer, 1996).
- [73] J. Gryko, R. F. Marzke, G. A. Lamberton Jr., T. M. Tritt, M. Beekman, and G. S. Nolas, *Phys. Rev. B* **71**, 115208 (2005).
- [74] G. C. Carter, L. H. Bennett, and D. J. Kahan, *Metallic shifts in NMR, Part I*, Progress in Materials Science, Vol. 20 (Pergamon, Oxford, 1977).
- [75] N. W. Ashcroft and N. D. Mermin, *Solid State Physics* (Saunders, Philadelphia, 1976).
- [76] Y. Guyot, B. Champagnon, E. Reny, C. Cros, M. Pouchard, P. Melinon, A. Perez, and I. Gregora, *Phys. Rev. B* **57**, R9475 (1998).
- [77] J. D. Dunitz, V. Schomaker, and K. N. Trueblood, *J. Phys. Chem.* **92**, 856 (1988).
- [78] A. Bentien, S. Johnsen, and Bo B. Iversen, *Phys. Rev. B* **73**, 094301 (2006).
- [79] X. Tang, J. Dong, P. Hutchins, O. Shebanova, J. Gryko, P. Barnes, J. K. Cockcroft, M. Vickers, and P. F. McMillan, *Phys. Rev. B* **74**, 014109 (2006).
- [80] C. R. Miranda and A. Antonelli, *Phys. Rev. B* **74**, 153203 (2006). References for reversible scaling Monte Carlo (RS-MC) method may be found in this paper.
- [81] I. Barin and O. Knacke, *Thermochemical Properties of Inorganic Substances* (Springer-Verlag, Berlin, 1973).
- [82] P. Flubacher, A. J. Leadbetter, and J. A. Morrison, *Philos. Mag.* **4**, 273 (1959).
- [83] I. Estermann and J. R. Weertman, *J. Chem. Phys.* **20**, 972 (1952).